

Submitted to: *Special Issue of IEEE Transactions of Geoscience and Remote Sensing*
on "*Emerging Scatterometer Applications*"

SEASONAL TO INTERANNUAL VARIABILITY IN ANTARCTIC SEA-ICE SURFACE MELT

Mark R. Drinkwater and Xiang Liu
Jet Propulsion Laboratory
California Institute of Technology
Mail Stop 300-323
4800 Oak Grove Drive
Pasadena, CA 91109, USA

Corresponding Author: Mark R. Drinkwater
Tel: +001 818-354 8189
Fax: +001 818-393 6720

Email: M.Drinkwater@jpl.nasa.gov

Final Manuscript Submitted:

March 13, 2000

Seasonal to Interannual Variability in Antarctic Sea-Ice Surface Melt

Mark R. Drinkwater, *Member, IEEE* and Xiang Liu
 Jet Propulsion Laboratory, California Institute of Technology
 4800 Oak Grove Drive, Pasadena, CA 91109
 (Email M.Drinkwater@jpl.nasa.gov)

Abstract - Satellite remote sensing time-series images are used to illustrate the spatial and temporal variability in Antarctic-wide sea-ice surface melting during the austral summer. Combinations of collocated data from the Active Microwave Instrument on board the ERS-1/2 spacecraft, RadarSat Synthetic Aperture Radar (SAR) and SSM/I passive microwave radiometer are used in characterization of the effects of surface melting on measured values of the normalized backscatter cross-section and brightness temperature, respectively. An algorithm is developed from observed signatures to map interannual variations in summer season melt onset and the cumulative number of melt days throughout each austral summer from 1992- 1998. Results indicate that Antarctic sea-ice surface melting is sparse and relatively short-lived, in contrast to the protracted Arctic summer melt season. Regions consistently experiencing melt periods of 15 days or longer duration are focused around the Antarctic Peninsula, primarily in the northwest Weddell and Bellingshausen Seas.

Keywords -Antarctic sea ice, melt onset, melt pond, microwave, radar, radiometer, ERS, NSCAT, SSM/I, SAR, scatterometer, seasonal variability, interannual variability, austral summer.

I. INTRODUCTION

Fundamental differences exist between Antarctic and Arctic sea-ice with respect to its spatial and temporal variability in response to seasonal atmospheric and oceanographic forcing. In summer, the Arctic Ocean basin remains populated by old, multiyear ice, surviving each melt season by way of its thickness, to subsequently thicken under autumn cooling and winter growth. Antarctica, however, has no widespread multiyear ice counterpart, and for the most part non-landfast sea ice experiences only one summer melt period before drifting into high oceanic heat-flux regimes and melting. Sea-ice dynamics regulate the maximum age of the ice cover, particularly in the Weddell and Ross Seas, where cyclonic ocean gyre circulations sweep sea ice northwards. The relative age and thickness of the residual autumn ice cover maintained in these gyres is a critical variable to the stability of the upper ocean in and around Antarctica. Summer sea-ice melt helps to freshen and stabilize the mixed layer. This provides a thermal barrier and prevents upward mixing of heat from beneath [1]. Furthermore, insulation afforded by a snow cover, found on summer sea-ice, prevents complete seasonal removal of the seasonal ice cover.

Around Antarctica, summer air temperatures rise only sporadically above 0°C. Consequently, classical surface melt ponds have rarely been observed on field experiments and the sea-ice surface typically retains a snow cover year-round. Conversely, Arctic summer surface melting results in the expression of melt ponds over up to 60% of the surface as the snow cover disappears completely. Meltwater infiltrates the warm, porous sea ice, flushing out its salt content to leave it relatively brine-free. The fact that the Antarctic snow cover is

retained throughout summer helps to insulate the ice, to maintain a relatively higher mean salinity in thicker ice, and to protect the sea ice from temporarily warm air temperatures [2].

This paper addresses whether surface melting plays a significant role in the decay and retreat of the Antarctic sea-ice cover during the summer months. A previous effort to monitor Antarctic ice-shelf surface melting applied passive microwave radiometer data [3]. Although summer melt duration has been estimated for Arctic sea ice using similar data [4], passive microwave algorithms often suffer in the high atmospheric water-vapor conditions frequently found over the Antarctic sea-ice cover. Thus, satellite microwave radar data are used here to estimate the timing of austral summer melt onset and the extent and duration of the melt season. These data were generated from two series of wind scatterometer measurements spanning several years. With continuous night and day operation, coupled with the all-weather imaging capability, scatterometer backscatter images are demonstrated to be an effective means of monitoring seasonal characteristics of the global sea-ice cover [5,6]. No other long-term, global radar time series presently exists nor is there other suitable proxy climate data available that could help characterize the spatial and temporal variability of Antarctic surface melting.

II. BACKGROUND

The first *in-situ* field observations of Antarctic austral summer sea-ice surface melt were made in the Bellingshausen Sea by Arctowski on Belgica in 1899 [7], and later by Wordie [8] during the ill-fated drift of Endurance in the Weddell Sea from 1914 to 1916. It has been 100 years since these pioneering ship drift experiments, yet little more is known about the spatial extent, duration, frequency of Antarctic seasonal surface melting of sea ice during the austral summer, or its interannual variability. Early explorers and modern-era surveys of the Weddell Sea alike [8A,9] have explicitly reported the absence of widespread, vigorous surface melt, as characterized by the formation of extensive melt ponds in midsummer in the Arctic [10]. Although bordered by a relatively warm ocean surface, energy balance calculations by [2] suggest that net surface heat fluxes over the Weddell Sea pack ice are insufficient to induce widespread, protracted surface melting. The appearance of melting on sea ice is particularly important as it modifies the albedo of the surface of the remaining ice and thus has a large impact on the radiative component of the energy balance during summer. With a winter to summer retreat in areal extent of the Southern Ocean sea-ice cover from 20×10^6 to 3×10^6 km², observed by SSM/I [11] and Scatterometer [6], the Antarctic sea-ice cover has a significant impact on the net albedo of the Southern Hemisphere.

The so-called “albedo-feedback” effect [12] results in Arctic

melt ponds and ultimate removal of a large fraction of sea-ice during the summer months. This feedback operates when snow surface melting reduces the mean spectral albedo of the surface from ~0.9 to 0.7 or less (via thermal alteration of snow grains and reduced reflectivity, and appearance of water in liquid phase) [13]. Increased absorption of short-wave and trapped long-wave radiation results in larger amounts of energy expended in melting of the snow and sea-ice surface and a further reduction in the spectral albedo. This positive feedback accelerates the removal of large expanses of Arctic ice too thin to survive an extended summer period of combined surface, lateral and bottom melt. In Antarctica, sea ice is completely surrounded at lower latitudes by ocean. Intuitively, therefore, summer storms are expected to be capable of delivering significant quantities of heat to the austral summer ice pack. Yet large regions of sea ice manage to survive the austral summer in spite of this and the relatively high ocean heat flux environment [1].

Previous work using microwave radar data have characterized Arctic summer ice melt at a variety of frequencies [10,14,15,16]. Based upon these observations, Winebrenner *et al.* recently reviewed observations of melting in Arctic satellite radar data [17]. Previous research dedicated to automated recognition of the expression of melting in radar data has primarily focused on the summer decrease in perennial ice backscatter evident in Arctic high-resolution SAR data. Since the early Seasat satellite radar observations of summer melting [14,15], no attempts have been made to exploit scatterometer data for this purpose. In their summary of the state-of-art Winebrenner *et al.* [17] concluded that "much work on automated recognition and mapping of seasonal transitions on sea-ice remains to be done".

It was the objective of this work, therefore, to develop a methodology for exploiting the long-term scatterometer microwave image time series for deriving melt information. The primary criteria were (i) that the derived products must be of practical value to the current generation of General Circulation Models (GCMs), and (ii) that they contain sufficient spatial and temporal information with which to interpret the seasonal progression of melting and the duration of melt season. Importantly, the resulting gridded data products must be applicable to prescribing seasonal changes in the albedo boundary conditions presently used in GCMs. Without such information it is impossible to correctly predict the response of the climate system to these sea-ice feedbacks.

The following sections describe first the satellite, *in-situ*, and meteorological data sets which were used in the study. Second, an error modeling study is undertaken to quantify the effects and impact of wind speed variability during low summer ice concentrations. Third, a description of the algorithm and methods employed in melt detection are provided. Fourth, results of measuring the seasonal and interannual variations in surface melting are discussed, together with the conclusions of this study.

III. DATA SETS

Both active and passive satellite microwave remote sensing data were used in this melt study together with *in-situ* field measurements and meteorological data. Data were collected

through a number of carefully coordinated, simultaneous field and satellite data acquisitions between 1992 and 1997. As the most suitable overlapping *in-situ* and remote sensing data sets exist for the Weddell Sea, we restrict our description of direct surface observations of melting to this region. Figure 1 shows the area of focus in the northwest Weddell Sea where a variety of data samples were selected to provide radar and radiometer characterizations of surface melting.

A. Satellite Data

Wind Scatterometer

The ERS wind scatterometer (EScat) is a sub-system of the active microwave instrument (AMI) flown on the ERS-1 and 2 series of satellites since 1991. This instrument measures VV-polarized, C-band (5.3 GHz) normalized backscatter (σ^0) along a single 500 km-wide swath, with an absolute accuracy of 0.2 -0.3 dB [18,19]. On August 16, 1996, the NASA scatterometer (NSCAT) was launched. In contrast to EScat, it measured Ku-band (13.995 GHz) backscatter at VV and HH polarizations along a 600 km-wide swath on each side of the satellite. NSCAT σ^0 measurements are estimated to be of comparable accuracy to the ERS instrument [20]. Unfortunately, due to failure of the ADEOS platform, data were only acquired until June, 1997. Both EScat and NSCAT swath data were processed using the scatterometer image-reconstruction with filtering (SIRF) algorithm [21]. Enhanced resolution image data were produced with a 6-day temporal window, and resampled onto a polar stereographic grid. The final products comprise Antarctic 6-day mean images at 3-day intervals having a pixel spacing of 8.8 km and 4 km, for EScat and NSCAT respectively. Images span the period since 1992.

Time series were derived of the mean 40° incidence-angle-normalized backscatter coefficient, $\sigma^0(40^\circ)$ (hereafter A) from each of the numbered boxes in Figure 1. These data are used to illustrate the seasonal and interannual variability of sea ice in the northwestern Weddell Sea and to characterize the typical backscatter transitions taking place as the ice undergoes seasonal surface melt. Later, the image data are exploited to extrapolate these regional melt characteristics in an Antarctic-wide melt detection algorithm.

Synthetic Aperture Radar

High-resolution synthetic aperture radar (SAR) snapshot images are also used in this study to identify ice-surface characteristics, to evaluate open-water wind conditions, and to make estimates of local ice concentration. Summer ERS-1 data acquisitions from February and March 1992 have previously been analyzed and published [22]. These data were collected during the drift of Ice Station Weddell [23] and illustrate the end of the summer melt and freeze-up transition period in 1992 (see Figure 2). Further pairs of overlapping, ascending and descending ERS-1 SAR orbit data were acquired on February 11 and 14 (shown in Figure 1 and Figure 3a) and February, 12 and 15, 1995, each spanning several hundred kilometer long swaths. Figure 1 shows two descending ERS-1 SAR mosaics (dashed) from February 11 and 14 on a polar stereographic grid projection. These crossed the open ocean limit of the marginal ice zone (MIZ) at around 65° S into high concentration ($> 95\%$) perennial ice south of 67° S (in

Figure 3a)

Additional RADARSAT ScanSAR images were acquired throughout December, 1996 and January, 1997. The location of the wide-swath mosaic on January 12 and 13, 1997 is shown in Figure 1. Together with the ERS-1 SAR images and EScat data, these RADARSAT images ensure that *in-situ* and remote sensing examples are available from the summers 1991/92, 1994/95, and 1995/96.

SSM/I

Passive microwave data were acquired by the Special Sensor Microwave/Imager (SSM/I) series of instruments flown on the Defense Meteorological Satellite Program (DMSP) satellite series from June 1987 through the present day. The primary sensor products used in this study are gridded 19.4 and 37 GHz v-pol brightness temperature image data obtained from the National Snow and Ice Data Center (NSIDC). Corresponding daily, polar stereographic gridded sea-ice concentration data [24] were also obtained at a pixel spacing of 25 km. For comparison, we reprocessed the data into 6-day average images at 3-day intervals in a similar manner to EScat images.

B. Meteorological Data

Meteorological data are useful to interpreting the microwave data and to understand the ice surface melting mechanisms. Daily heat flux and air temperature data were extracted from the NCEP/NCAR reanalysis data for the period from 1992-1997. These data are gridded products projected on a Gaussian grid, with a zonal 1.875° interval and a varying meridional interval of around 1.9° in the region shown in Figure 1. Data were extracted from grid points closest to the regions of interest, and averaged with a 6-day moving window at a sampling interval of 3 days.

Meteorological data recorded by various local Antarctic Peninsula (hereafter AP) stations and an automatic weather station (AWS) were acquired for the purposes of comparison with the image data and validation of the timing of melt onset (identified by labeled triangles in Figure 1). Air temperature datasets are shown in Figure 2 for (a) Marambio (M) from January 1, 1988 to December 31, 1997; (b) Faraday (F) from January 1, 1986 to December 31, 1995; and (c) the Larsen Ice Shelf AWS (L) from January 1, 1986 to November 30, 1995.

C. In-situ Data

Field measurements were made during the drift of Ice Station Weddell [23] during the period from February until June, 1992. Although this coincided with the early part of the 3-day ice-orbit phase of the ERS-1 time series, *in-situ* measurements were made between February and March which were coincident with both SAR and EScat data. Results of *in-situ* observations are described in greater detail in [25,26] and discussed in comparison with the remote sensing data in [22].

Further field measurements were acquired between 10-15 February, 1995 from H.M.S. *Endurance* [27]. The British Royal Navy icebreaker positioned herself to collect simultaneous *in-situ* data during the ERS-1 overpasses described in the previous section. One helicopter facilitated surface data collection while another was equipped for aerial photography. The 11th and 14th February descending pair of SAR swaths were acquired during

daylight (09:25hrs local time), thereby enabling detailed air-photo comparisons [28,29].

IV. ENVIRONMENTAL CONDITIONS

A. Seasonal Air Temperatures

Meteorological time series data from the peninsula stations in Figure 2 show the typical seasonal cycle in air temperatures. Marambio and the Larsen AWS indicate air temperatures rising from early October, typically through mid-November before the first appearance of positive values. Air temperatures typically quickly fall again during the months of February or March. The onset of the freeze-up varies considerably, with significant interannual variation.

On the western side of the AP, Faraday typically experiences warmer and longer summers and less intense winters than stations on the eastern side. Marambio, which has the most consistent long-term record on the eastern side, shows brief periods with summer air temperatures exceeding zero degrees, and longer spells of positive or melting degree days in 1993 and 1995. The Larsen AWS consistently experienced problems with calibration of air temperatures during the summer months. Nevertheless, the Larsen AWS helps to define the seasonal cycle in temperatures, particularly in 1995 when the *Endurance* field data were obtained. In these data the freeze-up occurs rapidly with air temperatures dropping below -10°C towards the end of February. The north-south seasonal air temperature gradient along the AP is also clearly evident, with typically 10°C difference between Marambio and Larsen in the period March through September.

B. Summer Ice Conditions

Summer ice conditions typical of the north west Weddell Sea are described by two SAR mosaics in Figure 3a and 3b. In February 1995 the mosaic shows an embayment in the ice margin with the outermost edge aligned east west at around 65° South. Box 15 remained partially covered by sea ice of low concentration ($< 50\%$) up until freeze-up, due to a northward extension in the ice edge (dashed line) off James Ross Island. This extension in the ice margin was delineated in the ascending orbit ERS-1 SAR mosaic obtained on February 12 and 15, 1995. Helicopter transects and aerial photographs along the white lines in Figure 3a (from [27]) indicate ice concentrations rapidly increased to over 85% within ~ 75 km of the ice edge. Sea ice south of 66°S latitude (such as box 13) had concentrations exceeding this value.

Surface melt is demonstrated to have a significant effect upon regional signatures in the northwestern Weddell Sea. *In-situ* observations of melting made in February 1995 explain the widespread reduction in A values in box 7, 8, 15, and 16. Figure 3c shows a vignette of an ERS-1 SAR scene obtained coincident to aerial photographs made from *Endurance* (centered on white spots). The air photograph indicates large melt ponds (up to 50m across) on the lower left edge of the large perennial ice floe [27]. Until this experiment, such melt ponds had never before been observed on Antarctic sea ice. Similar melt ponds are also observed on smaller ice floes (15-200m in diameter) seawards to within 2-3 km of the ice edge before floes became too small to

support them. Measurements also indicated that such perennial floes were typically 2.5-4m thick with a 2-15 cm deep snow cover [27].

Melt ponds do not appear to have a significant enough response at 23° incidence that they stand out in the high-resolution, SAR images. Nonetheless, due to the melt pond areal coverage in the photograph it is apparent that the average calibrated ice-floe backscatter coefficient is depressed from cold, winter values typical of old ice [30]. By the same token regional ice signatures in low-resolution, higher incidence-angle EScat data are expected to reflect this depression of typical sea-ice backscatter values as a function of the extent of ice floe surface melting.

Figure 3b shows contrasting ice conditions on January 12 and 13, 1997, with a distinctive coastal polynya and lower concentrations along the coast. In late December 1997 the ice margin retreated, leaving box 15 outside the ice margin. SAR images acquired two weeks earlier indicate marginal ice zone conditions with ice concentrations of about 15% in this box. The central sea-ice region around box 16 has an ice concentration of around 50%, while further to the south box 13 has a concentration exceeding 95%. In Figure 1, and to the lower left side of Figure 3b, box 1 indicates a control sample box on what was originally the northernmost piece of the Larsen Ice Shelf (LIS) or LIS-A. LIS-A disintegrated in 1992 and subsequently fast ice formed which remained in place until the end of December, 1995 [31]. The mosaic in Figure 3b successfully shows the situation just after break out of this fast ice. Box 1 was chosen because the time series data are effective in defining the melt period expressed on thick snow-covered sea ice. Furthermore, this sample region is close to Marambio, from which the air temperature record is plotted in Figure 2.

Figure 3b indicates the expression of melting on the Larsen B portion of the ice shelf (lower left image) as dark pixels. Further offshore, dark sea-ice floes surrounded by relatively brighter, deformed ice confirm the expression of surface melting. EScat and NSCAT images illustrate the progression of seasonal ice-shelf melting and its interannual variability [6]. Local ice-shelf melting is important as a means of confirming the effects of regional air temperatures along the peninsula.

V. REGIONAL SCATTEROMETER SIGNATURES

When interpreting the seasonal variations in EScat backscatter time series derived from the sample boxes in Figure 1, it is important to be able to quantify the effects of ice concentration, and fluctuating wind speed and air temperatures. Each may have an impact upon the regional mean backscatter measured by a scatterometer instrument.

A. Impact of Air Temperature

Previous work has demonstrated that at ice concentrations exceeding 95%, the modulation of the backscattering coefficient by wind speed and direction is negligible [22]. In this study, the relationship between EScat A values, the high-resolution SAR backscatter coefficient measurements of sea-ice, and *in-situ* wind and air temperature conditions were recorded at Ice Station Weddell (at around 71°S, 53°W). No correlation was observed between the satellite-measured backscattering coefficients and

wind, implying that the fetch-limited, wind-induced roughening effect on small leads was insufficient to cause significant bias in regional mean A values. The observed variability in SAR backscatter and EScat A values was instead highly correlated with air temperatures measured by the meteorological station at Ice Station Weddell and buoys surrounding the ice camp [22]. Furthermore, *in-situ* measurements by thermistors embedded within the sea ice [26] showed that the thermal gradient within the snow and sea ice determines the magnitude of the snow-ice interface reflection coefficient. In this manner, seasonal air temperatures regulate the regional backscatter of the summer sea-ice pack.

B. Modeling of Wind Impact

At relatively lower ice concentrations (< 90%) the wind can have a non-negligible contribution to the regional averaged A values. Here we use a simple model to demonstrate the effects of wind on the weighted mean backscatter coefficient at varying concentrations of typical perennial and seasonal sea ice. The intention is to quantify wind effects in ice conditions more typical of the summer ice margin in Figure 3, where ice concentrations vary between 15 and 90 %, and where summer surface melting is experienced. The model is based on the following equation:

$$\sigma_{tot}^o = A_i \sigma_{ice}^o + (1 - A_i) \sigma_{ocean}^o \quad (1)$$

where A_i is fractional coverage of ice, σ_{ice}^o is the regional mean sea-ice backscatter coefficient, σ_{ocean}^o is the backscatter coefficient of the wind-roughened leads or open water fraction, and σ_{tot}^o is the weighted mean regional backscatter coefficient. The value of σ_{ocean}^o is computed using the CMOD4 transfer function, which characterizes the backscatter as a function of wind speed, incidence and azimuth angle [32]. Model results in Figure 4 are computed for a fixed 40° incidence angle, to correspond with EScat A values. An azimuth angle of 0° (relative to the wind direction) is arbitrarily chosen, since the largest effective wind modulation of backscatter occurs when the viewing geometry is aligned downwind and the wind and wave propagation direction are similar. Two extreme cases are chosen, first in Figure 4a for varying concentrations of typical winter perennial ice (with relatively high backscatter coefficient) and second in Figure 4b for varying concentrations of melting perennial ice or seasonal ice (each with similar backscatter values).

Figure 4a shows the wind speed influence upon backscatter coefficient for typical winter perennial sea ice (where $\sigma_{ice}^o = -8$ dB after [30]). In the austral winter, typical wind speeds of 0 - 15 ms^{-1} are observed [22]. In this range, the modeled regional mean backscatter coefficient increases and tends to σ_{ice}^o values at 100% sea-ice concentrations. Higher ice fractions per unit area imply greater mean backscatter values, because in general large proportions of perennial ice have higher backscatter values than the remaining wind-roughened open water up to wind speeds of 17 ms^{-1} . For concentrations higher than 0.6, the backscatter varies within ± 2 dB. Backscatter values vary by a maximum of ± 4 dB for ice concentrations ranging from 0.4 to 1 over the entire wind speed range.

In contrast, for austral summer melt conditions in Figure 4b,

or typical seasonal sea-ice backscatter values (where $\sigma_{ice}^o = -15$ dB), there is a larger increase of ~ 4 dB in σ_{tot}^o values as wind speeds increase. At wind speeds below 7 ms^{-1} , regional mean backscatter values remain depressed below typical mean A values of the surrounding sea ice. However, the wind-speed threshold at which mean backscatter may be biased high is lower for seasonal or melting ice. High wind speeds ($> 15 \text{ ms}^{-1}$) can cause increases in the effective regional mean backscatter exceeding $+5$ dB at low ice concentrations (< 0.4). This is particularly important when considering surface melting in marginal ice zones with low summer concentrations (such as box 15 in Figure 3a). Nevertheless, since the impacts of limited fetch and stable boundary-layers are disregarded here, the modeled extrema in σ_{tot}^o may be considered upper bounds to the effect of wind upon EScat-observed A values.

VI. MELT DETECTION ALGORITHM

As stated in the previous sections, the effect of summer melt is observed as a spatial and temporally varying reduction in scatterometer A values. The spatial pattern of this reduction is expressed in two EScat A sub-images in Figure 5, in the northwest Weddell Sea, in the vicinity of the AP. Figure 5a indicates a mean 6-day image for the peak melt period in 1995, between February 5 and 10. The color table values were optimized in Figure 5 to indicate the melt-front. Melting ice surfaces are observed to have values below -20 dB, at the boundary between light blue and dark green colors. The pattern of melting is relatively coherent, extending approximately east west, with a finger of values below -25 dB extending to the southwest onto the southern portion of the LIS. In some locations, the impact of surface melting upon the backscatter is patchy with a large 100×100 km isolated patch of perennial ice (beneath the descending SAR swath on February 14, 1995) which until 10 February appears to have survived the effects of melting. As snow-depth has a large impact upon insulating the surface of the sea-ice [33,34], areas with large fractions of thick snow-covered perennial ice react slowest during brief periods of warming. This effect can be exaggerated by the layered snowcover found on perennial sea-ice floes in the Weddell Sea [35]. Deep, low thermal conductivity snow can support a strong negative temperature gradient [34], that effectively conducts heat away from the snow/air boundary under brief periods of net positive (downward) heat fluxes.

Figure 5b indicates the period of simultaneous SAR and *in-situ* measurements from HMS *Endurance*. By 14 February the residual patch of perennial ice sampled *in-situ* by helicopter, had begun to melt, with a reduction in regional A values of ~ 8 dB. According to observations in Figure 3c, the appearance of surface melting and of extensive melt ponds resulted in the reduction of typical perennial ice A values (~ -8 dB) to values below -16 dB. Meanwhile, the general northward movement of the melt front in other areas indicates that the southernmost air temperatures are slowly cooling. LIS A values in the vicinity of the Larsen AWS are observed to have increased by over 10 dB, while cooling of perennial sea-ice areas to the south of Marambio restores local signatures back to their former A values.

Figure 6 shows the 1994-95 melt transition in box 15 data. Melt onset is characterized by an abrupt decline in backscatter of

several decibels over a contiguous time period exceeding a week. This decline occurred at a time when the ice margin was far north of this box location and ice concentration was at its highest. In 1994/95 a reduction in backscatter of 7 dB occurred over a period of 21 days (or seven images spaced at intervals of 3 days) in the region observed to be melting in Figure 3a. The accompanying plot of $\delta A/\delta t$ in Figure 6b indicates that the time derivative of A remains negative for a period of 8 consecutive images, or 24 days. The combination of these two criteria has the advantage of filtering out small rapid fluctuations occurring as a result of the combination of oscillating spring air temperatures, variable ice concentrations and mid-winter storms.

Machine-automated algorithms have been developed for estimation of melt onset dates in the Arctic using low-resolution (100m) ERS-1 SAR imagery [16,17]. Here, an equivalent melt-detection algorithm is developed to detect the onset of melting and the number of cumulative melting days using EScat and NSCAT scatterometer images of Antarctic ice. For easy comparison, higher resolution NSCAT data were resampled into the same grid as EScat. A 15×15 pixel two-dimensional spatial Gaussian filter ($\sim 130 \times 130$ km) was first applied to the images to reduce orbit swath noise. Noise is manifested particularly in EScat data of the Weddell and Ross Seas as a result of large spatial and temporal variability in sampling due to conflicting SAR operation of the ERS-1/2 AMI instrument within direct broadcast range of the O'Higgins (in Figure 1) and McMurdo SAR receiving stations.

For this study, data processing was limited to pixels in the EScat image between the sea-ice margin (determined by the SSM/I-derived 15% ice-concentration contour) and the Antarctic coastal mask. The backscatter change between two consecutive images was iteratively computed at each pixel location and stored. At each time step temporal pixel differences were computed and stored in memory for 7 contiguous floating point images (spanning an 18 day period for EScat and NSCAT data), requiring approximately 60 mB dynamic memory. For each pixel, the melt onset date was determined when the following criteria were met. In the case of Antarctic sea ice, the A value decrease from one image to the next must exceed 0.5 dB, and the total decrease within the 7 consecutive images window was no less than -3 dB. After each sea ice pixel was searched and checked for melting, the array is shifted to the next image, another set of 7 consecutive images is loaded and the process repeated.

To test and validate the approach, the algorithm was applied to a series of examples. Firstly the melt-detection criteria were applied to the time series at the location $64^\circ\text{S } 56^\circ\text{W}$ in Figure 6. The algorithm automatically selected November 15, 1994 (day 319 or 1994.87) as the date of melt onset. Figure 2 suggests that this date coincides with air temperatures increasing and remaining for the first time consistently above -5°C at the Marambio coastal station. To further validate the expression of melt onset in the regional sea-ice signatures of the northwest Weddell Sea we selected data from "control" boxes on the nearby LIS. Ice-shelf signatures offer the advantage of ruling out possible effects due to sea-ice concentration variability or advection of varying ice types (with different backscatter) through the boxes. Figure 7 shows the results of plotting a blow-up of the 1996/97 melt season for LIS boxes (numbered 1-4), together with contrasting time series from sea-ice boxes 15 and

20. The upper panel indicates a large dynamic range in A values as a result of austral summer melt as far south as 68° S. Decreases of 10 to 20 dB occur relative to the stable winter values, and melting is confirmed by concurrent SSM/I 19 GHz v-polarized T_b values tending to 273 K [6,28]. Figure 7a indicates the sharp definition of the melt onset in boxes 1-4 as an initial 10 dB drop in A values. For comparison, the algorithm-retrieved melt onset is shown as a cross for each of the boxes. The algorithm correctly recognizes identical onset dates in each of the time series despite the different mean backscatter values of ice-shelf and fast-ice regions. False identification of initial brief periods of melt (due to strong cyclonic activity prior to onset of ice shelf melting), such as that observed in northernmost boxes 1 and 2, was avoided by adjusting the temporal-windowing method described earlier. The different intensity of the melt signal observed on the ice shelves is likely due to differences in the intensity of melting as a consequence of different boundary layer and energy balance conditions [36].

Figure 7b shows accompanying data for boxes 15 and 20, together with the Marambio air temperature record in Figure 7c and the accompanying NCEP net heat fluxes in Figure 7d. Just prior to the detected onset of melt, air temperatures increased from -20°C to -2°C in the space of 2 weeks. At the same time, NCEP net surfaces reverses from typical mid-winter values of below -20 Wm^{-2} to become positive. The sign convention used for net flux here is such that positive implies a net downward flux. As local surface air temperatures approach 0°C at Marambio, melt onset is observed in box 15. The coincidence of net positive heat flux with these air temperatures implies melting only begins when a surplus of energy at the surface coincides with air temperatures close to zero. At this point in time, the snow surface must be isothermal, such that heat supplied from the atmosphere to the surface will change snow from solid to liquid phase. The melt onset (shown as a star in Figure 7b and d) corresponds with the dip in A values observed at 1996.83 in Figure 7a in boxes 1 and 2 on the LIS. After a short period of melt, air temperatures briefly dip below -5°C before approaching 0°C for the remainder of the summer. Throughout the summer, brief positive excursions in air temperatures are accompanied by dips of around 3dB in A values in box 15. A values decline overall as a combination of the effects of seasonal melt and variations in ice concentration to the point where open water conditions are evident in Figure 7b.

In contrast, box 20 shows a different characteristic seasonal trend (Figure 7b) with a summer increase in A . This box is beyond the southernmost point of penetration of the NCEP seasonal 0°C isotherm in the western Weddell Sea. Similar distinctive summer increase in backscatter in February 1992 accompanied seawater flooding of the snow-ice interface of many perennial snow-covered ice found in this region [26]. Snow-covered perennial ice floes surrounding Ice Station Weddell (ISW) increased their σ_{vv} values in austral summer as a result of ice-surface flooding at the base of the snow [22]. Since air temperatures at this latitude are too cold for snow-surface melting, the snow must insulate the ice sufficiently for it to be warmed by heat supplied from beneath. At temperatures above a threshold of approximately -5°C [37] the ice becomes permeable. If the snow cover is deep enough for an isostatic imbalance [33] then it may flood with seawater through open

brine drainage channels, causing a widespread increase in σ_{vv} [28].

In-situ data from ISW in 1992 [26] confirm that summer increases in A values are not caused by atmospherically induced surface melting. Box 20 results in Figure 7b and other such sample boxes in Figure 1 are similarly interpreted as experiencing no melting. Support for this conclusion is provided in Figure 4b, where low ice concentrations and sustained high wind speeds are necessary throughout the summer season to cause the observed increase (Figure 7b) from -17 to -10dB. Importantly, seasonal increases in backscatter are consistently observed in each of the sample time series south of box 9 (*i.e.* boxes 10, 11, 12, 18, 19, and 20), implying that the effects of surface melting rarely penetrate south of 67° S on the sea ice during the period shown. Though contrary to box 3 and 4 ice-shelf observations of melting in Figure 7a, patterns of low backscatter values in EScat images (Figure 5) clearly show localized regions of surface melting fringing the Antarctic Peninsula, rather than extending out large distances into the Weddell Sea ice pack.

VII. RESULTS

A. Melt Onset Patterns from EScat and NSCAT

The melt algorithm was first applied to map the spatial pattern of seasonal melt onset for the entire image time series between 1992 and 1997. To check the consistency of melt onset retrieval between frequencies and instruments we first compared results from simultaneous EScat and NSCAT observations. Figure 8 shows a comparison of results from each instrument for the 1996-97 austral summer. Blues and greens represent melt onset during November and December, while browns, reds, oranges and yellows highlight successively later melt onset during January, February or March, respectively. The SSM/I-derived 15% ice concentration contour is indicated for November 8, 1996 (day 313) to delineate the ice extent prior to melt onset. An inner line delineates the 15% ice concentration contour at the end of the algorithm run on March 14, 1997 (day 73).

Figure 8 indicates that the frequency difference between NSCAT and EScat has little impact upon the detection of melt onset, and that the melt process causes a similar spatial response at both wavelengths. The algorithm is relatively robust, sensing regionally consistent dates of melt onset throughout the ice cover. The primary difference is that Ku-band data have a higher spatial resolution and capture a larger dynamic range, and thus are more sensitive to the appearance of melting signatures. This sensitivity leads to more widespread NSCAT recognition of melt onset in parts of the central Ross Sea, particularly in locations experiencing only brief bouts of surface melt, or mixed pixel effects.

To validate the spatial patterns we have compared the time-tagged colored patches in Figure 8 (indicating contiguous regions of detected melt onset) with gridded NCEP data (described in section 3.2). NCEP reanalysis products were used exclusively in the peninsula region, as these data are expected to have the largest number of station meteorological data assimilated into the products. Figure 9 shows the contoured net surface heat flux field, and the shaded region corresponds to

positive air temperatures at melt onset. Relatively warm air and large positive net heat fluxes during early summer are confined to the Weddell Sea ice margin region, with a southernmost extent in the AP region. The location of enclosed flux contours with values exceeding 140 W/m^2 match closely with the blue melt onset region in Figure 8.

Buoy deployment results from Vihma *et al* (In Press) indicate heat fluxes measured by meteorological buoy 5895 during the 1996-1997 austral summer. From November 1, 1996 (day 305) onwards, buoy 5895 experienced large positive net surface heat fluxes and air temperatures close to and periodically exceeding 0°C . Melt onset is reported the scatterometers on November 9, 1996 (day 313) at the buoy location (66°S 35°W). At this time, the buoy indicated combined peaks in net radiation and turbulent sensible heat flux. These two characteristics are well reproduced in meteorological analysis data from ECMWF and NCEP, but a third characteristic of positive latent heat flux indicated by the buoy at melt onset is incorrectly reproduced. These inaccuracies suggest that the turbulent latent heat flux component of the current analysis products are not to be trusted, and that net heat fluxes are biased low at melt onset by as much as 20 W m^{-2} . Furthermore, the balance of fluxes over the buoy ice-floe surface suggests that the average net flux during the 1 month period November 1 to December 31 was approximately 20 W m^{-2} , with peaks of up to 50 W m^{-2} . This extended period of net downward heat flux implies a time lag of around 1 week before melting begins, and subsequently around 0.6 to 1.5 cm ice melt per day (i.e. 0.2 - 0.5 m over the course of November, 1996).

It has previously been demonstrated that for melting to occur in Antarctica surface air temperatures must be substantially higher than in the Arctic [2]. This condition is true because the air is typically drier under the influence of dry continental winds [38]. Under typical springtime relative humidities of $\sim 80\%$, the surface can tolerate higher temperatures without melting provided that advective heat loss by sublimation balances the large net radiation input at the surface. For melting, surface-layer temperatures must be substantially higher than in the Arctic, and at or above 0°C for the typical Bowen ratios (i.e. the ratio of sensible to latent heat flux), wind speeds and humidities observed *in-situ*. Clearly it is rare for summer melting to occur even with a positive net heat flux. It occurs mostly near the ice margin where a source of warm, moisture-laden air exists. NCEP data also appear to indicate that the general conditions required are therefore a combination of large positive radiation balance, a combination of both positive sensible and latent turbulent heat fluxes (i.e. from the atmosphere to the surface), and air temperatures close to or above 0°C .

B. Seasonal Pattern of Melt Onset

Figure 8 indicates a roughly poleward melt onset progression as seasonal air temperature increase. Surface melt, however, is neither widespread nor spatially contiguous at any given instant of time during the summer, as is supported by *in-situ* observations of episodic warming [39]. Locations of melt patches appear linked to the locations of storm tracks supplying warm air masses and sufficient heat to induce only temporary surface melting. The pre-melt ice margin location and the ice margin corresponding to the end of the melt transition period,

indicate the distance of sea-ice margin recession during the melt season. Large portions of the sea-ice cover experience little or no surface melt during ice-edge recession, suggesting that the combination of episodic warm air advection and positive net heat fluxes play only a small role in removing sea ice from these regions in summer. Instead, ice extent in the northwestern Weddell Sea appears governed by ice advection. Despite early melt onset the ice edge shows minimal recession due to ice replenishment from the south.

The melt algorithm identifies what seem to be several false melt signatures. Indications of melt onset are observed, for instance, late in the summer of 1996-97, and in particular along the Ronne-Filchner ice-shelf front in the southern Weddell Sea. Although an automatic weather station on the Ronne ice shelf ("Limbert" at 72.42°S) reported some temperatures above zero, these did not appear to have been sustained long enough for melt onset. Instead, it is more likely that surface warming causes brine-volume increases and significant permittivity changes in the relatively young, high-salinity ice forming in that active ice-shelf polynya location [40]. The result would be a summer decline in thin-ice backscatter which mimicks that of melting, particularly on newly-formed expanses of undeformed, level ice.

C. Spatial Pattern in Cumulative Melt Days

The cumulative number of days of melt are recorded by the algorithm for a given pixel from melt onset onwards. Since fluctuations in A values are common, periods of positive time derivatives (i.e. inferred cooling), such as in Figure 6b, are rejected. Figure 10 shows comparative results for the number of cumulative melt days recorded in each scatterometer data set. Notably, in order to obtain similar results for C- and Ku-band frequencies, the melt criteria had to be relaxed for EScat data (from -3 to -1 dB drop). This is partially attributable to increased noise, reduced resolution, and lower sensitivity of the C-band A values to the appearance of moisture in the snow (i.e. reduced dynamic range).

Protracted summer surface melting in a specific region is rare and typically short-lived. Instead of long periods with depressed backscatter coefficients, the summer is characterized by large fluctuations in backscatter indicating melting and freezing cycles [28]. This behavior is not unique to the sea ice, but is also observed on neighbouring ice shelves, where meteorological station data (Figure 2) confirm such temperature fluctuations. The total cumulative melt days recorded by both instruments confirm that the only sea-ice locations experiencing protracted vigorous melting (exceeding 30 days) in 1996-97 were regions bordering the Antarctic Peninsula, in the Weddell and Bellingshausen Seas, and East Antarctic coastal regions. The southernmost melting region is observed in the Ross Sea, while the anomalous point in the Amundsen Sea (with values exceeding 20 days) is discovered to correspond with the top surface of the large, drifting Thwaites iceberg (B10A).

D. Characteristics of the Annual Cycle

Time series of the mean A values were extracted from EScat pixels falling within each of the sea-ice boxes in Figure 1, using a similar method to [28,29]. Figure 11 shows values from boxes of two different sizes, and distances from the AP. These were

selected to show variability indicative of seasonal and interannual changes in the characteristics of the snow and ice floe surfaces, together with the proportions of ice types advected through each region. In each plot the upper panel shows the mean A values (solid line) and one standard deviation bounds. Generally, box 9 in Figure 11a indicates slightly larger variance than box 22 in Figure 11b, since the larger the box the greater the variance in ice conditions. The middle panel of each plot indicates the annual cycle, and the anomaly cycle in the lower panel shows the residuals after removing the smoothed 5-year mean.

The two examples indicate differences in the mean annual cycle as a consequence of the varying impact of melting, combined with the advection of varying fractions of seasonal or perennial ice through each box. Figure 11a shows a characteristic dip in October as summer approaches, and as the concentration of perennial ice dwindles as it is advected northwards out of the western Weddell Sea. The anomaly time series indicates that melting had a large impact on the summer signatures in 1992/93, 1994/95, and 1996/97, and summer oscillations in A in these time series indicate melt/freeze cycling. In the intervening years (1992, 1994, and 1995), a strong February-March peak in A indicates that larger than normal quantities of perennial ice were advected through the region. Corroborative field evidence was collected during the WWGS '92 shipborne field experiment, for instance, when swarms of large floes of thick perennial ice with > 1 m deep snow, were observed exiting the western Weddell Sea [35].

The time series from box 22 shows a large contrast to box 9. It was selected because it experiences only brief periods of summer melting and is covered by high concentrations of sea ice throughout the period shown. This box is too far to the east to experience varying mixtures of perennial and seasonal sea ice, and this reflected in the lack of a consistent pattern to the seasonal cycle. The long-term mean backscatter value reflected by the stable mean annual value of -14.5 dB in the central panel of Figure 11b is typical of deformed first-year ice [30,40]. Because of the flat-line characteristic of its annual cycle, box 22 serves as a unique indicator of small dynamic anomalies in this part of the Weddell Sea, as well as highlighting the anomalies resulting from periodic melt events such as occurred at the end of February, 1996.

E. Interannual Melt Patterns

Figures 12 and 13 compare the interannual variability in melt patterns deduced from the EScat data record. Each have five panels indicating a single melt season, with areas of color-coded melt and white regions signifying no melt. Figure 12 shows that most years generally exhibit a southward melt-onset progression (from blue to red, to orange and then yellow). This causes early melt onset detection around the tip of the Antarctic Peninsula (*i.e.* at the lowest latitude ice margin) and melting extending eastwards along the sea-ice margin in the northern Weddell Sea, and westwards along the coast into the Bellingshausen Sea. The combination of melt algorithm results and SSM/I ice concentrations also indicate that the retrievals in the Weddell Sea occurring later in January and early February are indeed surface melting.

More southern sea ice regions tend to experience later melt

onset, as the sea-ice margin recedes southward. However, there is an exception to this rule, with early season melting consistently experienced in the Ross Sea. The melt onset algorithm also identifies isolated patches of late-season melt in the southern Weddell Sea (in February-March, 1997). Though this ice is clearly not melting from above, such circumstances could occur in smooth, thin ice regions when ocean heat fluxes warm the ice significantly enough to increase the permittivity of the ice surface. The result would be to increase the reflectivity and to cause reductions in the A values, and possibly false melt onset detection.

Sea ice around East Antarctica demonstrates extremely rapid recession, with the result that melt onset is detected on the narrow annulus of remaining sea ice. In all years except 1993-94, coherent bands of similar melt onset may be traced around the ice margin in Figure 12. The cumulative melt days results shown in Figure 13 help to visualize the regions where seasonal melting has the largest impact. Consistent surface melting occurs between 30°E to 120°E , for around 12 days except during the anomalous 1993-94 summer. Some of this anomaly may result from a number of regions of missing data during the first half month of January in 1994 such that no cumulative melting was detected. However, that alone does not appear to explain some of the large differences in melt onset, for instance.

The cumulative melt summary demonstrates that although there is significant interannual variation in melting, there are a number of locations around Antarctica which experience a consistently larger number of melt days (> 15) in a summer season. Results imply consistent summer melting around the Antarctic Peninsula, with a more southern extension of melting on the western flank around into the Bellingshausen Sea. Coastal sea-ice regions of East Antarctica with more than 15 cumulative melt days are less frequent or extensive. The only extended melting is observed in the Amery basin in 1992/93 and 1996/97.

VIII. CONCLUSIONS

Our results indicate that ERS-1/2 (C-band) and NSCAT (Ku-band) scatterometer image data are applicable to monitoring the large-scale surface characteristics of Antarctic sea ice. The radar backscatter coefficient A at 40° is sensitive to changes in reflectivity resulting from austral summer melting, and thus A values can be exploited in mapping surface melt. In May 1999 the QuikScat scatterometer was successfully launched. This instrument has no conflict with SAR data and recent data acquisitions indicate that it can be used for future Ku-band retrievals of sea-ice melt

A melt detection algorithm was developed and applied to scatterometer images collected over the period 1992-99, spanning both ERS and NSCAT missions. Resulting data provide valuable information about the interannual variability in Antarctic surface melt and insight into the contribution of the atmosphere to the austral summer ice retreat. Patterns appear to exist from year-to-year in atmospherically induced ice-floe surface melt. Coincident NCEP surface fluxes indicate that algorithm identified melt regions correspond with locations where a surplus of energy at the surface coincides with air temperatures close to or above -5°C . Such cases imply that heat delivered by the atmosphere and solar radiation is expended in surface melting, by the transformation of snow from solid to

liquid phase.

Seasonal trends in EScat σ^0 time series are explained primarily by a combination of variations in air temperature and advection of different ice types and concentrations into or out of the study boxes. Results indicate significant interannual variability occurs in the duration and intensity of the melt season, particularly in the northwest Weddell Sea. The austral summers of 1992/93 and 1994/95 were relatively warm, each with earlier and more extended melt seasons. The 1995 appearance of melt ponds coincided with the rapid disintegration of northern sections of the LIS and landfast ice between James Ross Island and the peninsula [31], and the calving of a spectacular iceberg from LIS close to box 2. Though February 1995 field observation of Antarctic melt ponds coincided with these occurrences, the appearance of similar melt periods in other years suggest that melt ponds may have been more widespread in the Antarctic Peninsula region in recent years. Continued warming presently occurring in this area is expected to have the most significant impact by increasing the frequency of melt ponds, thus leading to albedo feedback and potentially dramatic changes in the patterns of decay of the summer sea-ice margin in this region.

Summer-season surface processes are demonstrated to influence microwave radar data in consistent yet distinctive ways depending on whether the sea ice lies north or south of the seasonal isotherm corresponding to snow melting. Observations of increases in backscatter in many of the southern Weddell Sea sample boxes indicate the widespread nature of summer flooding processes leading to upward meteoric ice growth, more commonly known as snow-ice [22,28]. Since most thermodynamic models do not adequately represent this process, our results are expected also to shed new light on the seasonality and regionality of this unique Antarctic summer upward-ice-growth process. Further studies will optimize the present algorithm to track widespread increases in backscatter as a function of surface flooding.

Antarctic sea-ice responds quite differently from its Arctic counterpart during the summer season. Atmospherically led austral summer surface melting appears far less extensive in time or space than is experienced in the Arctic. Our results reiterate that atmospherically induced surface melting and resulting albedo feedback is not the dominant sea-ice removal mechanism. Instead, a combination of ocean heat flux and summer short-wave radiation absorbed by the ocean surface (in small lead fractions) rapidly disposes of most of the sea-ice cover. This confirms previous observational and numerical findings which suggested that the retreat of the Antarctic summer ice margin is not simply regulated by the atmosphere, but rather by a balance between ocean heat flux, atmosphere, and sea-ice dynamics [8].

The Thwaites iceberg (B-10A) drifting in the Amundsen Sea in 1996/97 provides an intriguing example of surface melt. The iceberg's top surface apparently experienced over 15 more days melt than surrounding sea ice at sea-level, thereby highlighting the existence of a strong temperature gradient in the lower atmosphere. Due to a fairly ubiquitous summer Antarctic inversion, cold stable air near the surface normally inhibits downward mixing of warmer air aloft. Icebergs stand higher in the inversion layer. As a result they encourage turbulent downward mixing of warm air and are therefore more

susceptible to summer surface melt. Unlike the surrounding sea ice, the iceberg surfaces do not deteriorate rapidly to the point where the signature of melt is erased. Future studies should identify the general circulation patterns and atmospheric boundary layer conditions that lead to some ice areas being more susceptible than others to surface melt.

Future studies will combine large-scale satellite-tracked sea-ice kinematics data with these interannual melt time series (e.g. [42]). Dynamical information such as opening/closing are essential to quantifying advective and dynamic influences upon the backscatter variability. On this basis, smart algorithms can be developed to more accurately extract thermodynamically regulated sea-ice characteristics from such radar time-series data.

ACKNOWLEDGMENT

ERS-1/2 SAR images were obtained through ESA Project AO1.PIP.ANT3 and Scatterometer data were delivered by IFREMER and analyzed as part of ESA Project AO2.USA.119. RADARSAT SAR data products were acquired from the Alaska SAR Facility through CSA/NASA ADRO Project 164, and SSM/I gridded data were supplied by the National Snow and Ice Data Center. NCAR/NCEP are acknowledged for providing meteorological reanalysis data products, and the British Antarctic Survey for Antarctic weather station data. Doug Low is acknowledged for his important contribution to the analysis of the ERS Wind Scatterometer data. MRD and XL completed this work at Jet Propulsion Laboratory, California Institute of Technology under contract to the National Aeronautics and Space Administration. Funding was provided by Dr. Prasad Gogineni of NASA Code YS (RTOP 621-21-02) and the JPL NSCAT Project Office.

REFERENCES

- [1] Martinson, D.G., and R.A. Iannuzzi, Antarctic ocean-ice interaction: implications from ocean bulk property distributions in the Weddell Gyre. In M.O. Jeffries (Ed.) *Antarctic Sea Ice: Physical Processes, Interactions and Variability*, Antarctic Research Series, 74, 243-271, American Geophysical Union, Washington, D.C., 1998.
- [2] Andreas, E. L., and Ackley, S. F., On the differences in Ablation Seasons of Arctic and Antarctic Sea Ice, *Journal Atmospheric Science*, 39, 440-447, 1982.
- [3] Ridley, J., Surface Melting on Antarctic Peninsula Ice Shelves Detected by Passive Microwave Sensors, *Geophys. Res. Lett.*, 20,23, 2639-2642, 1993.
- [4] Smith, D.M., Observation of Perennial Arctic Sea Ice Melt and Freeze-up Using Passive Microwave Data, *J. Geophys. Res.*, 103, C12, 27,753-27,769, 1998.
- [5] Drinkwater, M.R., D.G. Long, and D.S. Early, Enhanced Resolution Scatterometer Imaging of Southern Ocean Sea Ice, *ESA Journal*, 17, 307-322, 1993.
- [6] Long, D.G., and M.R. Drinkwater, Cryosphere Applications of NSCAT Data, *IEEE Trans. Geosci. and Remote Sens.*, Vol. 37, 3, May 1999.
- [7] Arctowski, H., Les Glaces: Glace de Mer et Banquises. Resultats du Voyage du S.Y. Belgica en 1897-1898-1899, *Rapports Scientifiques*, Vol. 5., J.E. Buschmann, Antwerp, [Trans., NTIS AD 881 363], 3-55, 1908.

- [8A] Wordie, J.M., Shackleton Antarctic Expedition, 1914-1917: The natural history of pack ice as observed in the Weddell Sea, *Trans. Roy. Soc. Edinburgh*, 52, 795-829, 1921.
- [8] Ackley, S.F., Mass balance aspects of Weddell Sea pack ice, *J. Glac.*, 24, 90, 391-406, 1979.
- [9] Gow, A.J., S.F. Ackley, K.R. Buck, and K.M. Golden, Physical and structural characteristics of Weddell Sea pack ice, *CRREL Report*, 87-14, 1987.
- [10] Gogineni, S.P., R.K. Moore, T.C. Grenfell, D.G. Barber, S. Digby, and M.R. Drinkwater, The Effects of Freeze-up and Melt Processes on Microwave Signatures, In *Microwave Remote Sensing of Sea Ice*, (Ed.) F.D. Carsey, American Geophysical Union, Geophysical Monograph 28, Chapter 17, 329-341, 1992.
- [11] Gloersen, P., W.J. Campbell, D.J. Cavalieri, J.C. Comiso, C.L. Parkinson, and H.J. Zwally, Arctic and Antarctic sea ice, 1978-1987: satellite passive-microwave observations and analysis. *NASA SP-511*, Washington DC, National Aeronautics and Space Administration, 1992.
- [12] Curry, J.D., J.L. Schramm, E.E. Ebert, Sea Ice-Albedo Climate Feedback Mechanism, *J. Climate*, 8, 240-247, 1995.
- [13] Maykut, G.A., The Surface Heat and Mass Balance, In *The Geophysics of Sea Ice*, (Ed.) N. Untersteiner, 395-463, Plenum, New York, 1985.
- [14] Carsey, F.D., Summer Arctic Sea Ice Character from Satellite Microwave Data, *J. Geophys. Res.*, 90, C3, 5015-5034, 1985.
- [15] Drinkwater, M.R., and F.D. Carsey, Observations of the late-summer to fall transition with the 14.6 GHz SEASAT scatterometer, *Proc. IGARSS '91 Symposium*, Vol. 3, IEEE Catalog #CH2971-0, June 3-6, 1991, Espoo, Finland, 1597-1600, 1991.
- [16] Winebrenner, D.P., E.D. Nelson, and R. Colony, Observations of Melt Onset on Multiyear Arctic Sea Ice using the ERS 1 Synthetic Aperture Radar, *J. Geophys. Res.*, 99, 11, 22425-22441, 1994.
- [17] Winebrenner, D.P., D.G. Long, and B. Holt, Mapping the Progression of Melt Onset and Freeze-up on Arctic Sea Ice using SAR and Scatterometry. In C. Tsatsoulis and R. Kwok (Eds.), *Analysis of SAR Data of the Polar Oceans*, Chapt. 7, 129-144, Springer-Verlag, Berlin, 1998.
- [18] Attema, E.P.W., P. Lecomte: The ERS-1 and ERS-2 Wind Scatterometer, System Performance and Data Products, *Proc. IGARSS '98*, IEEE International Geoscience and Remote Sensing Symposium Proc., 4, 1967-1969, 1998.
- [19] Lecomte P., W. Wagner, ERS Wind Scatterometer Commissioning and in-Flight Calibration, In *Proc. of a Joint ESA-Eumetsat Workshop on Emerging Scatterometer Applications - From Research to Operations*, Oct. 5-7, 1998, ESTEC, Noordwijk, The Netherlands, ESA SP-424, Nov. 1998.
- [20] Tsai, W., J.E. Graf, C. Winn, J.N. Huddleston, S. Dunbar, M.H. Freilich, F.J. Wentz, D.G. Long, W.L. Jones: Postlaunch Sensor Verification and Calibration of the NASA Scatterometer, *IEEE Trans. Geosci. and Remote Sens.*, Vol. 37, 3, May 1999.
- [21] Early, D.S., and D.G. Long: Resolution Enhancement of Scatterometer Data, *IEEE Trans. Geosci. Rem. Sens.*, In Press.
- [22] Drinkwater, M.R., and V.I. Lytle: ERS 1 Radar and Field-Observed Characteristics of Autumn Freeze-Up in the Weddell Sea, *J. Geophys. Res.*, Vol. 102, No. C6, 12593-12608, 1997.
- [23] Gordon, A.L., and Ice Station Weddell Group of Principal Investigators and Chief Scientists, Weddell Sea Exploration from Ice Station, *Eos*, 74, 121, 1993.
- [24] Cavalieri, D.J., P. Gloersen, and W.J. Campbell. Determination of sea ice parameters with the NIMBUS-7 SMMR, *J. Geophys. Res.*, 89(D4), 5355-5369, 1984.
- [25] Fritsen, C., V.I. Lytle, S.F. Ackley, and C.W. Sullivan, Autumn bloom of Antarctic pack ice Algae, *Science*, 266, 7824-7827, 1994.
- [26] Lytle, V.I., and S.F. Ackley, Heat flux through sea ice in the Western Weddell Sea: convective and conductive transfer processes, *J. Geophys. Res.*, 101, 8853-8868, 1996.
- [27] Low, D., The Validation of ERS-1 Summer SAR Data for Antarctic Summer Sea Ice, Unpublished M. Sc. Thesis, 143pp., 1995.
- [28] Drinkwater, M.R., X. Liu, D. Low, and P. Wadhams, Interannual Variability in Weddell Sea Ice from ERS Wind Scatterometer, *Proc. of a Joint ESA-Eumetsat Workshop on Emerging Scatterometer Applications - From Research to Operations*, 5-7 October 1998, ESTEC, Noordwijk, The Netherlands (ESA SP-424, Nov. 1998), 119-123, 1998a.
- [29] Drinkwater, M.R., X. Liu, and D. Low, Interannual Variability in Weddell Sea Ice from ERS Wind Scatterometer, *Proc. IGARSS '98*, Seattle, Washington, 6-10 July, 1998., IEEE Catalog # 98CH36174, Vol. 4, 1982-1984, 1998b.
- [30] Drinkwater, M.R., Satellite Microwave Radar Observations of Antarctic Sea Ice. In C. Tsatsoulis and R. Kwok (Eds.), *Analysis of SAR Data of the Polar Oceans*, Chapt. 8, 145-187, Springer-Verlag, Berlin, 1998a.
- [31] Rott, H., P. Skvarca, and T. Nagler, Rapid Collapse of the Northern Larsen Ice Shelf, Antarctica, *Science*, 271, 788-792, 1996.
- [32] Stoffelen, A., and D. Anderson, Scatterometer Data Interpretation: Derivation of the Transfer Function CMOD4, *J. Geophys. Res.*, 102(C3), 5767-5780, 1997.
- [33] Massom, R.A., M.R. Drinkwater, and C. Haas, Winter Snow Cover on Sea Ice in the Weddell Sea, *J. Geophys. Res.*, 102, C1, 1101-1117, 1997.
- [34] Massom, R.A., V.I. Lytle, A.P. Worby, and I. Allison, Winter Snow Cover Variability on East Antarctic Sea Ice, *J. Geophys. Res.*, 103(C11), 24837-24855, 1998.
- [35] Drinkwater, M.R., and C. Haas, Snow, Sea-ice and Radar Observations during ANT X/4: Summary Data Report, *AWI Berichte aus dem Fachbereich Physik*, 53, Alfred Wegener Institut für Polar- und Meeresforschung, July 1994, 58pp., 1994.
- [36] Schneider, C., Energy Balance Estimates During the Summer Season of Glaciers of the Antarctic Peninsula, *Global and Planetary Change*, 22, 117-130, 1999.
- [37] Crocker, G.B., and P. Wadhams, Modelling Antarctic Fast Ice Growth, *J. Glaciology*, 35, 3-8, 1989.
- [38] Schwerdfeger, W., The climate of the Antarctic, *World Survey of Climatology*, Vol. 14, *Climates of the Polar Regions*, S. Orvig (Ed.), Elsevier, 253-355, 1970.
- [39] Andreas, E.L., Heat and moisture advection over Antarctic sea ice, *Mon. Weather Rev.*, 113, 736-746, 1985.
- [40] Drinkwater, M.R., Active Microwave Remote Sensing Observations of Weddell Sea Ice. In M.O. Jeffries (Ed.)

Antarctic Sea Ice: Physical Processes, Interactions and Variability, Antarctic Research Series, Vol. 74, 187-212, American Geophysical Union, Washington, D.C., 1998b.

[41] Drinkwater, M.R., X. Liu, and S. Harms, In Press, Combined satellite- and ULS-derived sea-ice flux in the Weddell Sea, *Annals of Glaciology*, 2000.



Mark R. Drinkwater (M'88) was born in Oldham, United Kingdom in 1963. He received a B.Sc. honours degree in physical Geography at the University of Durham in 1984 after specializing in remote sensing in glaciology, and subsequently a Council of Europe Diploma in Remote Sensing in Engineering from the University of Dundee in 1984. In 1988 he received a University of Cambridge Ph.D. degree in Geophysics for a Scott Polar Research Institute doctorate

research project on microwave radar remote sensing of polar ice.

Between 1987 and 1988 he worked in Cambridge as a consultant with Polar Oceans Associates, a U.K. Division of Science Applications International Corporation. Shortly thereafter, he joined the Jet Propulsion Laboratory (JPL), California Institute of Technology as a National Research Council Resident Research Associate, and from 1990 to 2000 was employed as a Research Scientist in the Ocean Science Research Element of the JPL Earth and Space Science Division. During that period of time he worked on a number of international projects with NASA, ESA, CSA and NASDA and participated in several polar expeditions. In May 2000 he joined the European Space Agency as Head of the Oceans/Ice unit of the Science Division at the European Space Research and Technology Centre in Noordwijk, The Netherlands. His professional interests involve present and future satellite missions for microwave remote sensing of the oceans and terrestrial ice sheets. Research focuses include geophysical data extraction from polar remote sensing data, inverse electromagnetic scattering models, and in coupling information derived from EM and thermodynamic models with massively parallel general circulation models for large-scale estimates of surface fluxes of heat and salt in the polar oceans. He has published over 40 refereed journal articles, and several book chapters. Dr. Drinkwater is a member of the IEEE, the Electromagnetics Academy, the International Glaciological Society, and the American Geophysical Union (AGU). He recently served for several years as an Associate Editor of AGU's *Journal of Geophysical Research, Oceans*.



Xiang Liu received a B.E. degree in Fluid Mechanics from Zhongshan University, P.R. China in 1983, a M.S. degree in Mechanical Engineering from the same University in 1986 and a M.S. degree in Physical Oceanography from Florida State University, FL in 1992. She is currently a software engineer with the Polar Oceanography group at the Jet Propulsion Laboratory, Pasadena, CA.

List of Figures

Figure 1. Weddell Sea map indicating, (i) numbered sample boxes for EScat and SSM/I time-series data; (ii) ERS-1 SAR strips (dashed) on February 11 and 14, 1995; (iii) RADARSAT ScanSAR strip (dot-dashed) on January 12 and 13, 1997; and (iv) meteorological stations (triangles) situated at Faraday (F), Marambio (M), and an automatic weather station on the Larsen Ice Shelf (L).

Figure 2. Antarctic station air temperature data from 1992-1995 at (a) Faraday (F); (b) Marambio (M); and (b) Larsen ice shelf (L) autonomous weather station (data courtesy British Antarctic Survey). Gaps indicate failures in the instrumentation, in particular at the AWS. Figure 1 shows the locations of these stations as solid triangles. Shaded regions indicate periods of in-situ data, and triangular symbols indicate timing of RadarSat SAR image acquisitions.

Figure 3a. ERS-1 SAR swaths over the northwest Weddell Sea on February 11 and 14, 1995. The large black box indicates the location of a simultaneous H.M.S. *Endurance* field experiment. White lines indicate coincident helicopter aerial photograph survey transects made across the marginal ice zone. Numbered boxes refer to sample regions shown in Fig. 1. The dashed line indicates the sea-ice margin.

Figure 3b. Wide-Swath RADARSAT SAR image mosaic (orbits 6213 and 6227) of the Larsen Ice Shelf and northwest Weddell Sea in January 1997. Dark regions indicate extensive melting on the Larsen B and C ice-shelf areas. Melting sea-ice floes appear as dark patches adjacent to the ragged margin of the ice shelf. The bright region of Jason Peninsula indicates higher elevations and colder air temperatures, and white patches at the bottom edge of the mosaic indicate the southern extent of surface melting in 1997.

Figure 3c. ERS-1 SAR sub-image (left panel) of a large perennial ice floe (approximately 6 x 7.5 km in size), situated 100 km inside the ice edge at 65.85°S 55.75°W in Fig 3a. A coincident aerial photograph (right panel), from the location of the black box, indicates surface melt ponds (courtesy D. Low).

Figure 4. Modeling of the effects of wind speed on the weighted mean regional backscatter coefficient at 40° incidence (A), for (a) typical winter perennial ice (-8 dB); and (b) typical seasonal ice, or melting summer ice (-15 dB). The legend indicates the mean backscatter at varying ice concentrations A_i .

Figure 5. EScat A images of the study region on (a) days 036 - 041 (5-10, February); and (b) days 045 - 050 (14-19, February), in 1995. White open boxes show overlapping SAR swath locations simultaneous to the 10-15 February, 1995 H.M.S. *Endurance* field experiment. Open triangles indicate meteorological station locations.

Figure 6. Melt onset in box 15 in the north-west Weddell Sea (64°S 56°W) in late 1994, expressed as; (a) mean A values (σ_{vv}^0) at 3-day intervals; and (b) their time derivative. Vertical dashed line indicates the beginning of the 1995 calendar year.

Figure 7. ERS-2 scatterometer time-series of A values from (a) Boxes 1, 2, 3, and 4 on the Larsen Ice Shelf, together with crosses indicating algorithm-detected melt onset dates. (b) shows A values from boxes 15 and 20; (c) 6-day running mean air temperatures at Marambio; and (d) 6-day mean NCEP net heat flux in boxes 15 and 20.

Figure 8. Algorithm-detected melt onset date in (a) ERS-2 (b) NSCAT data during the 1996-97 austral summer season. A color bar and legend indicate the day of year on which melting began.

Figure 9. NCEP 6-day mean net heat flux contours on November 14, 1996 (Day 319). The shaded area represents the region in which NCEP surface air temperatures exceed 0°C.

Figure 10. Cumulative surface melt days detected by (a) ERS-2; and (b) NSCAT data during the 1996-97 austral summer season. White areas indicate no melting.

Figure 11. Interannual time-series of EScat values from (a) box 9, and (b) box 22. The upper panel in each plot shows the mean A values, with dotted lines indicating 1σ standard deviation. The central panel indicates the mean annual cycle (dotted) and its six month running mean (solid), and the lowermost panel shows the anomaly cycle resulting from removal of the smoothed mean annual cycle.

Figure 12. Interannual variability in melt onset for (a) 1992/93, (b) 1993/94, (c) 1994/95, (d) 1995/96, and (e) 1996/97.

Figure 13. Interannual cumulative melt variability for (a) 1992/93, (b) 1993/94, (c) 1994/95, (d) 1995/96, and (e) 1996/97.

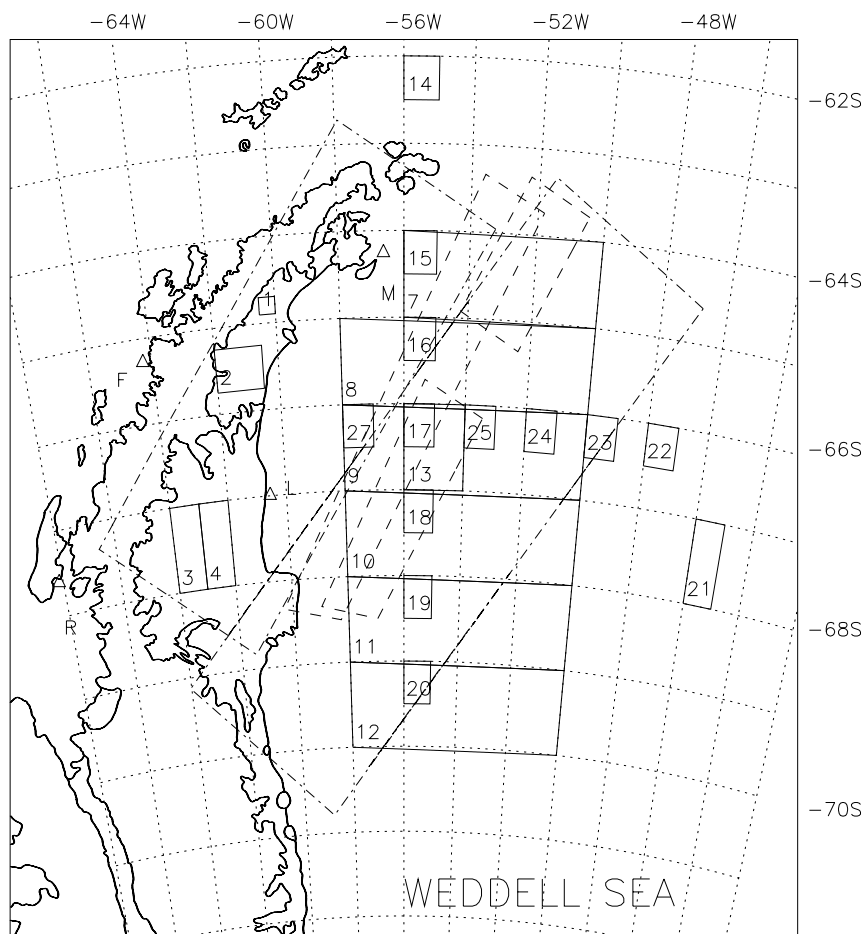


Figure 1. Weddell Sea map indicating, (i) numbered sample boxes for EScat and SSM/I time-series data; (ii) ERS-1 SAR strips (dashed) on February 11 and 14, 1995; (iii) RADARSAT ScanSAR strip (dot-dashed) on January 12 and 13, 1997; and (iv) meteorological stations (triangles) situated at Faraday (F), Marambio (M), and an automatic weather station on the Larsen Ice Shelf (L).

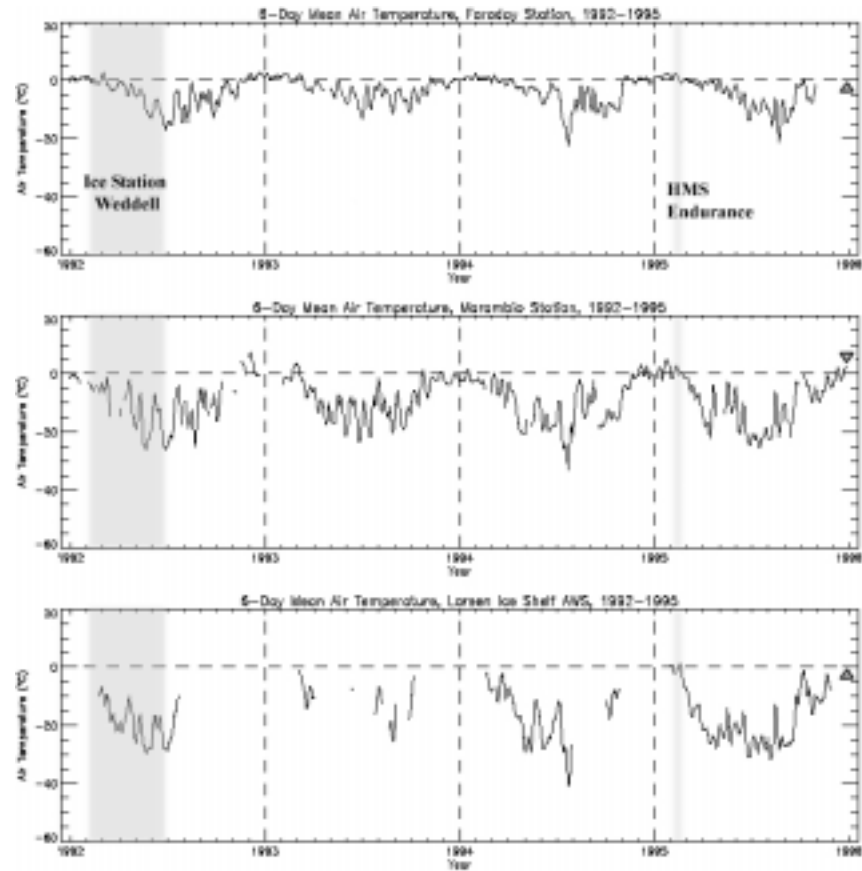


Figure 2. Antarctic station air temperature data from 1992-1995 at (a) Faraday (F); (b) Marambio (M); and (b) Larsen ice shelf (L) autonomous weather station (data courtesy British Antarctic Survey). Gaps indicate failures in the instrumentation, in particular at the AWS. Figure 1 shows the locations of these stations as solid triangles. Shaded regions indicate periods of in-situ data, and triangular symbols indicate when RadarSat SAR image acquisitions began (shown in Fig. 3).

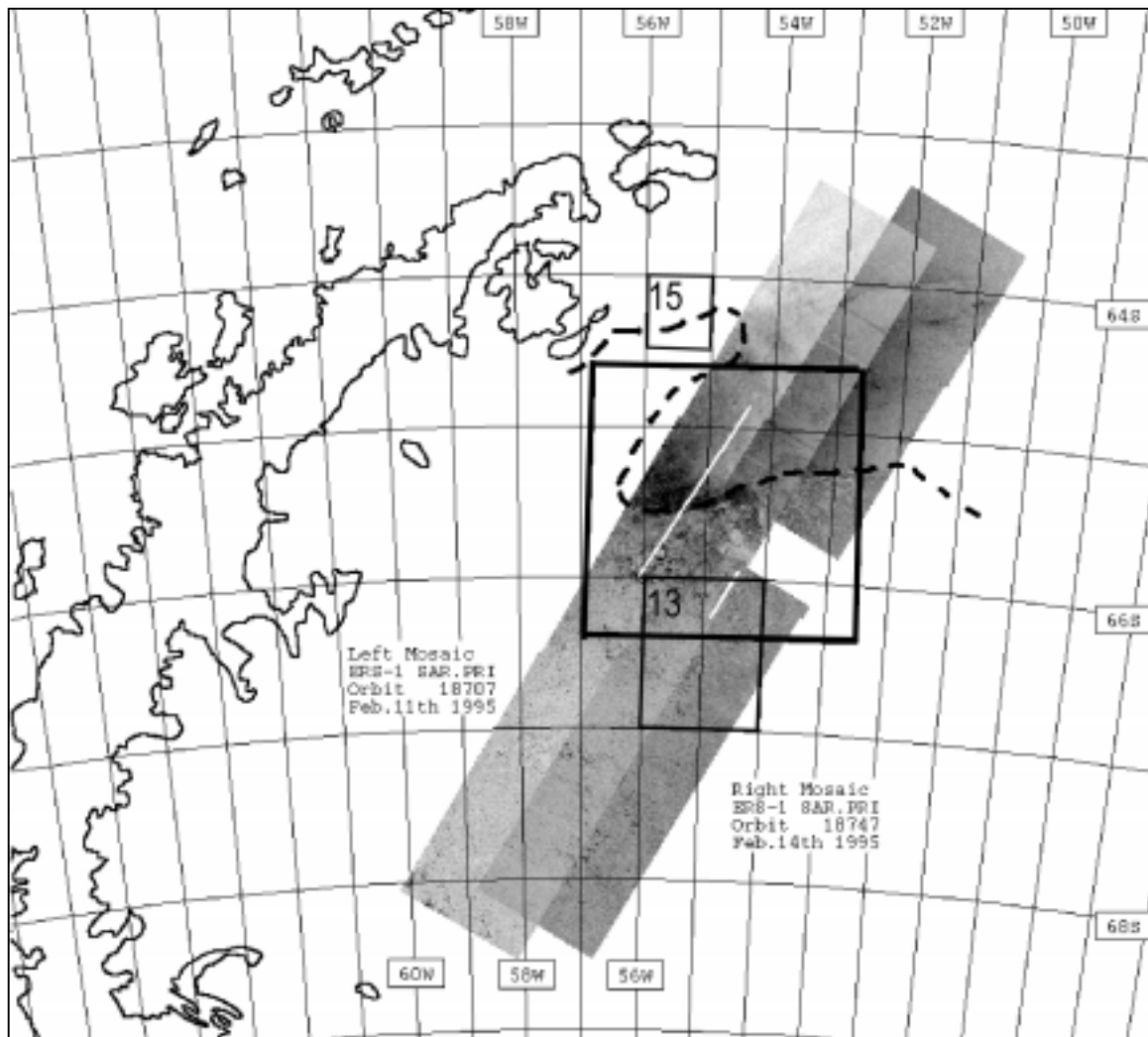


Figure 3a. ERS-1 SAR swaths over the northwest Weddell Sea on February 11 and 14, 1995. The large black box indicates the location of a simultaneous H.M.S. *Endurance* field experiment. White lines indicate coincident helicopter aerial photograph survey transects made across the marginal ice zone. Numbered boxes refer to sample regions shown in Fig. 1. The dashed line indicates the sea-ice margin.

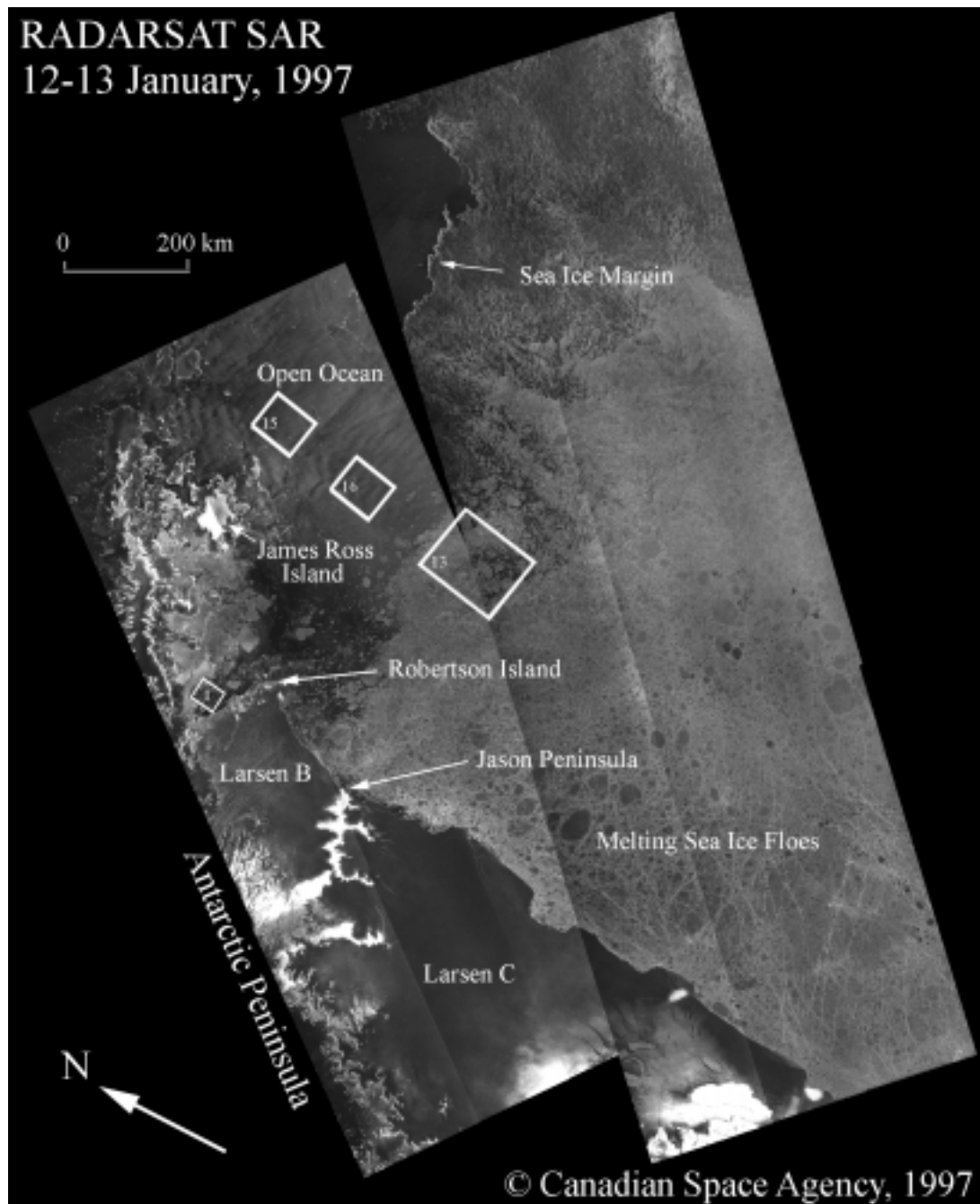


Figure 3b. Wide-Swath RADARSAT SAR image mosaic (orbits 6213 and 6227) of the Larsen Ice Shelf and northwest Weddell Sea in January 1997. Dark regions indicate extensive melting on the Larsen B and C ice-shelf areas. Melting sea-ice floes appear as dark patches adjacent to the ragged ice-shelf margin. The bright region of Jason Peninsula indicates colder air temperatures at higher elevations, and white patches at the bottom edge of the mosaic indicate the southern extent of surface melting.

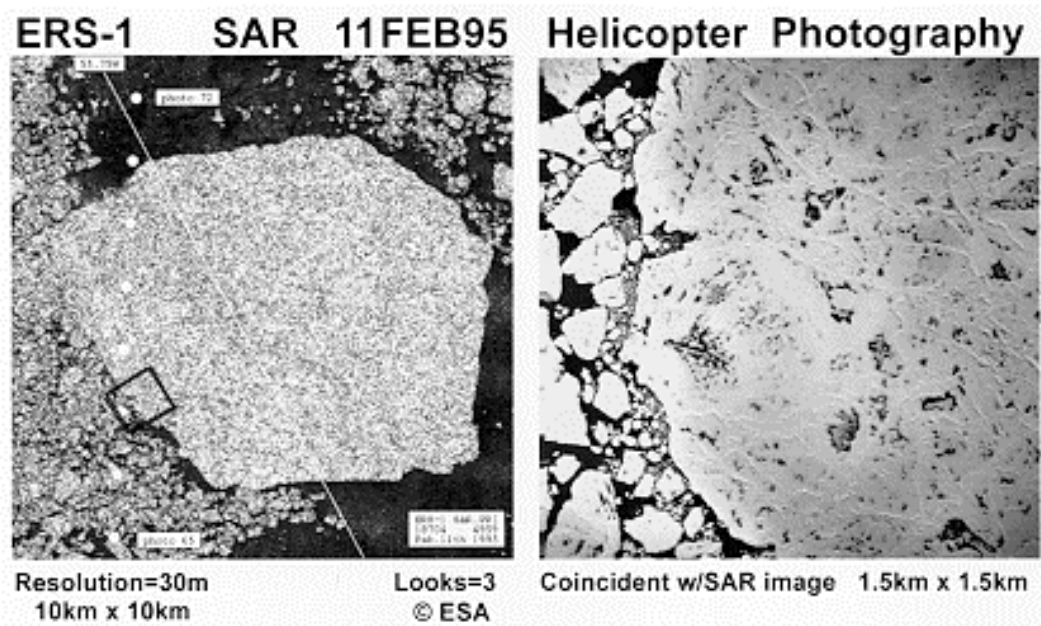
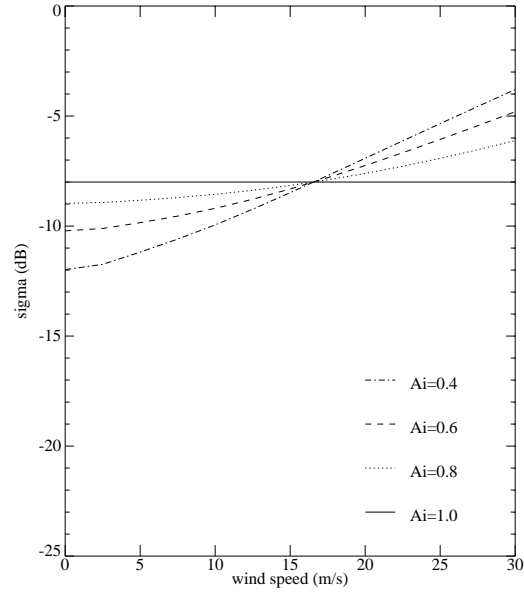


Figure 3c. ERS-1 SAR sub-image (left panel) from Fig 3a mosaic; and coincident aerial photograph (right panel) from black box indicating surface melt ponds (courtesy D. Low).

a.



b.

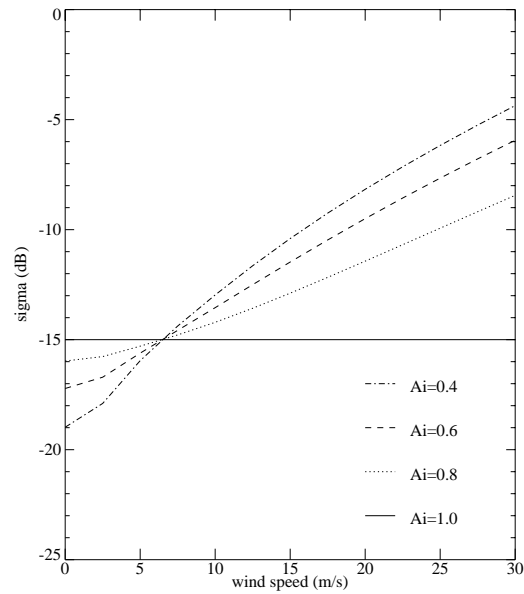
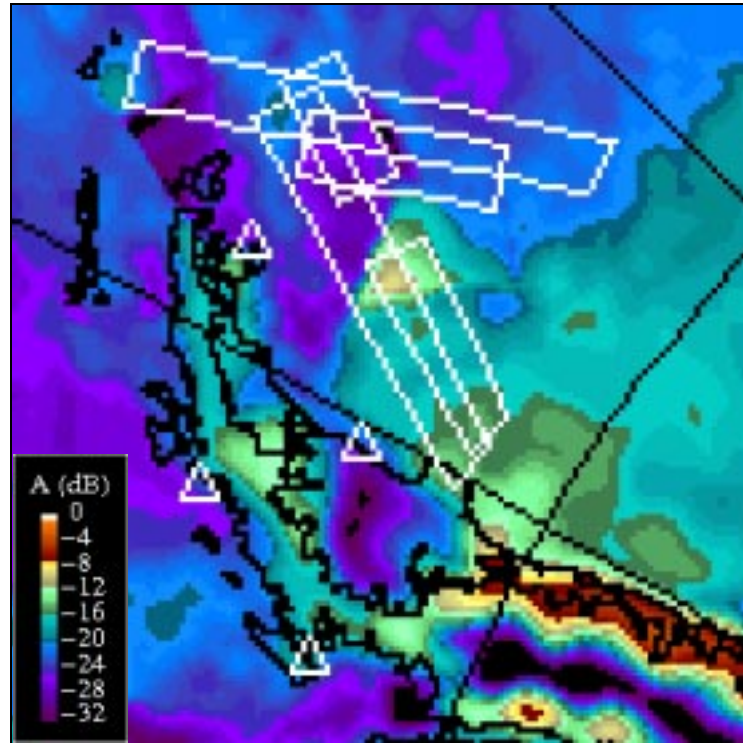


Figure 4. Modeling of the effects of wind speed on the weighted mean regional backscatter coefficient at 40° incidence (A), for (a) typical winter perennial ice (-8 dB); and (b) typical seasonal ice, or melting summer ice (-15 dB). The legend indicates the mean backscatter at varied ice concentrations A_i .

a.



b.

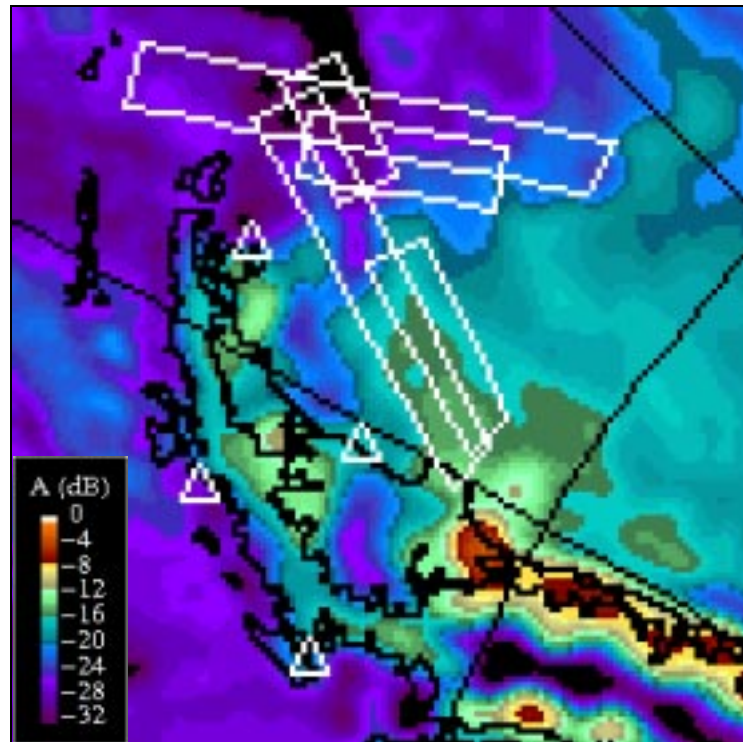


Figure 5. EScat A images of the study region on (a) February 5-10, 1995 (days 36-41); and (b) February 14-19, 1995 (days 45-50). White open boxes show overlapping SAR swath locations simultaneous to the 10-15 February, 1995 H.M.S. *Endurance* field experiment. Open triangles indicate meteorological station locations.

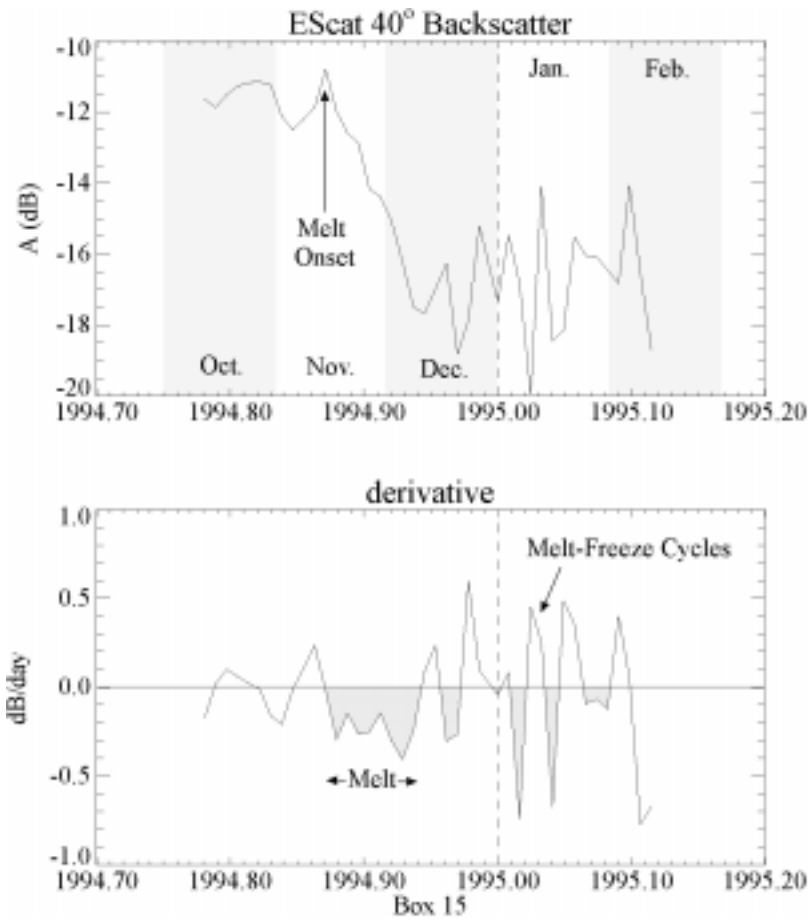


Figure 6. Melt onset in box 15 in the north-west Weddell Sea (64°S 56°W) in late 1994, expressed as; (a) mean A values (σ_{vv}^0) at 3-day intervals; and (b) their time derivative. Vertical dashed line indicates the beginning of the 1995 calendar year.

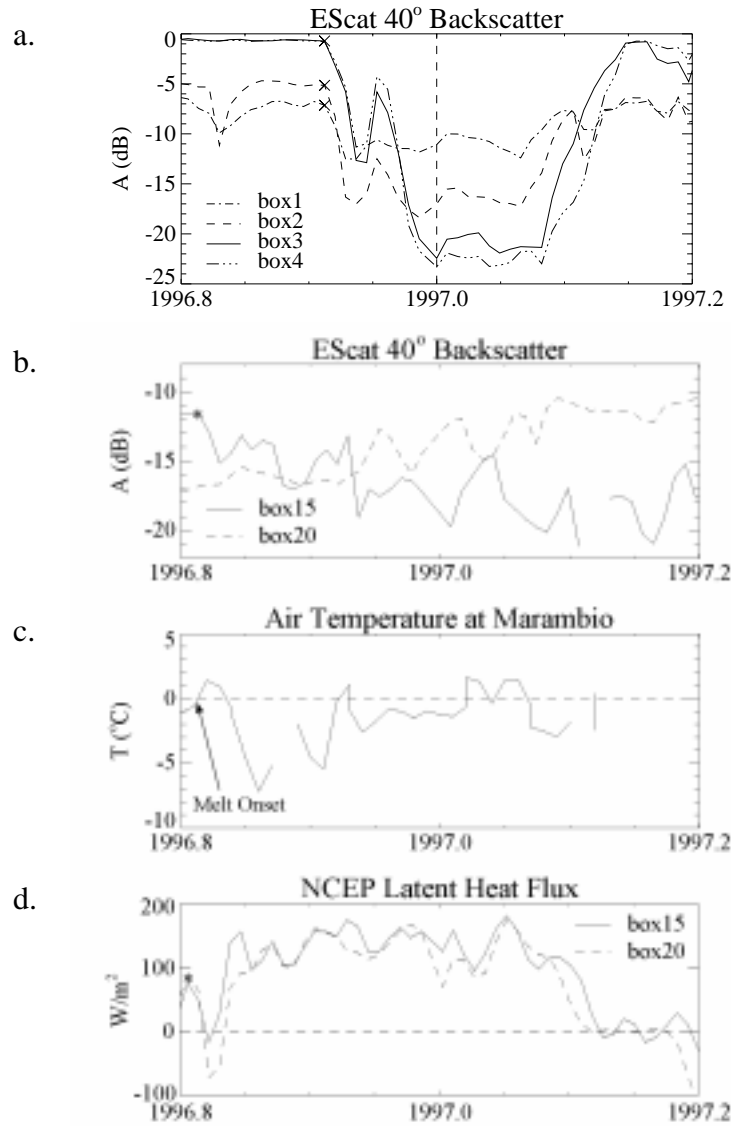


Figure 7. ERS-2 scatterometer time-series of A values from (a) Boxes 1, 2, 3, and 4 on the Larsen Ice Shelf, together with crosses indicating algorithm-detected melt onset dates. (b) shows A values from boxes 15 and 20; (c) 6-day running mean air temperatures at Marambio; and (d) 6-day mean NCEP net heat flux in boxes 15 and 20.

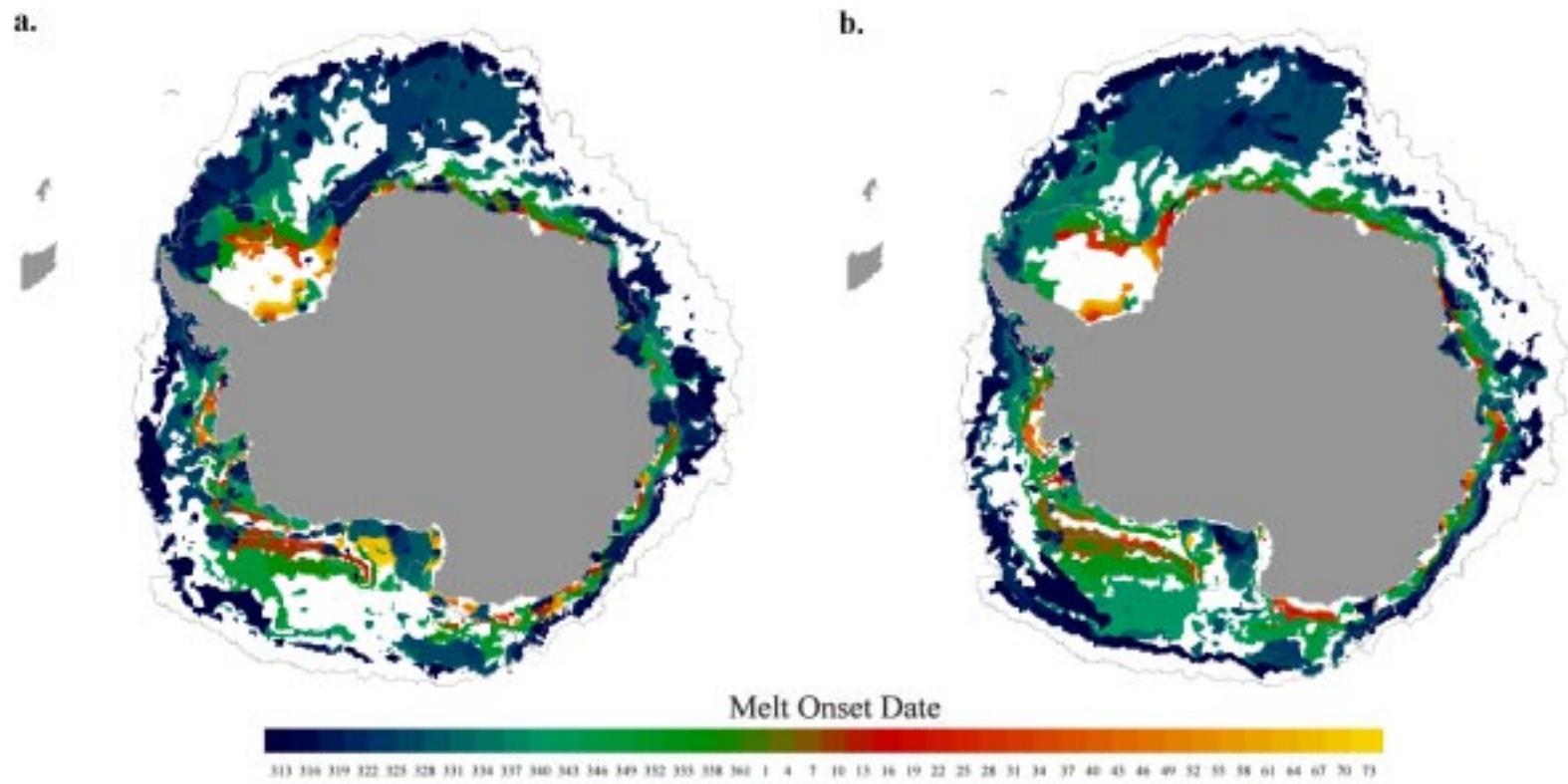


Figure 8. Algorithm-detected melt onset date in (a) ERS-2 (b) NSCAT data during the 1996-97 austral summer season.

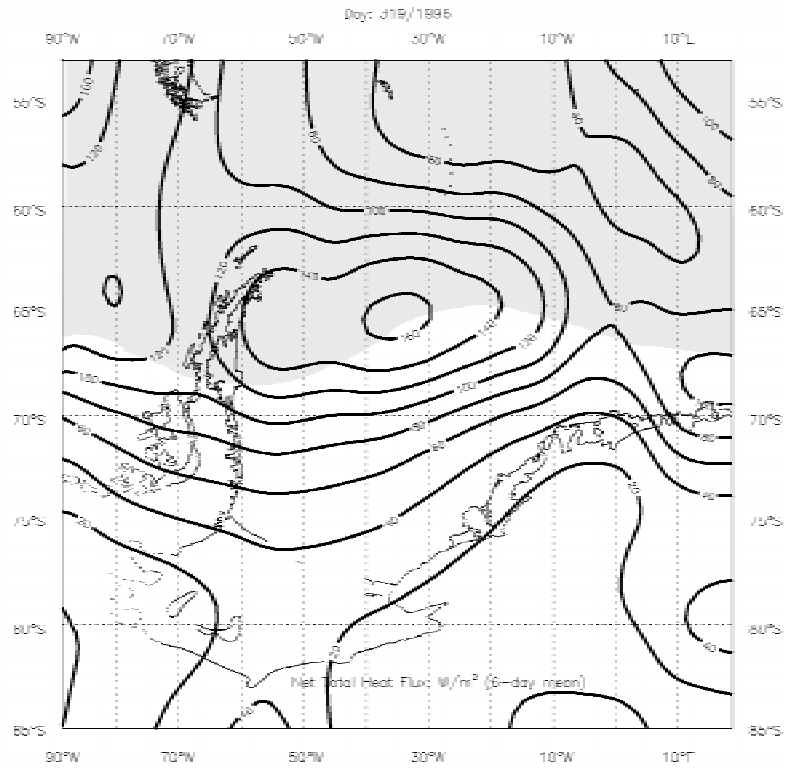
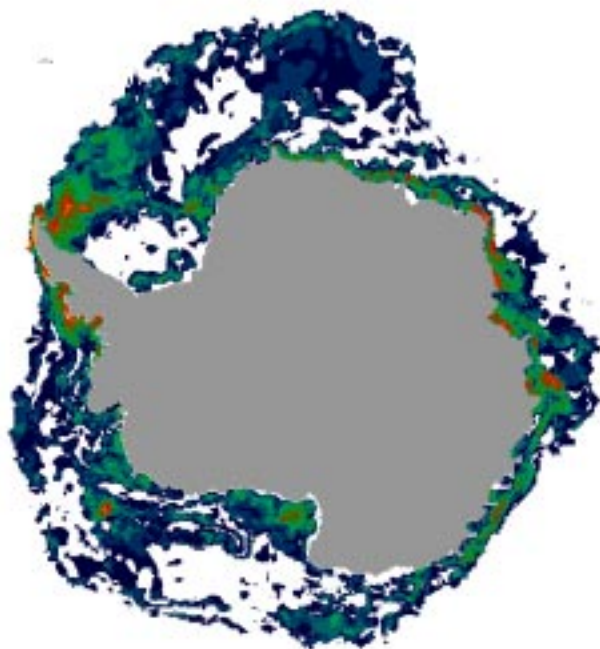


Figure 9. NCEP 6-day mean net heat flux contours on November 14, 1996 (day 319). The shaded area represents the region in which NCEP surface air temperatures exceed $0^{\circ}C$.

a.



b.

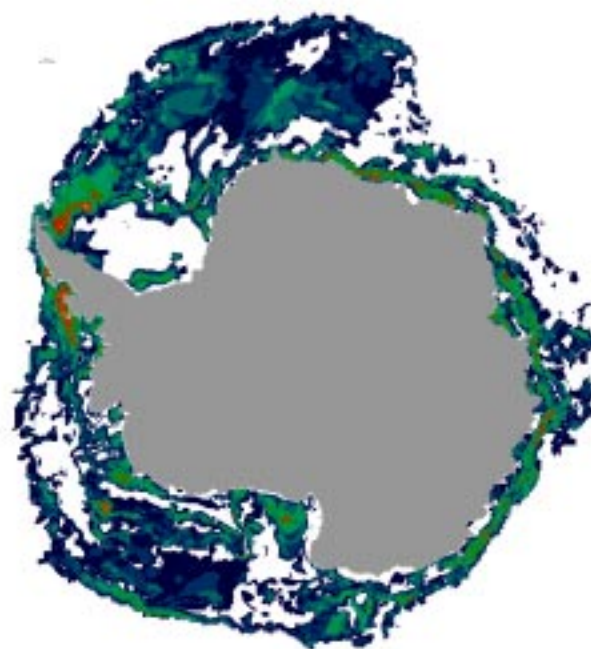
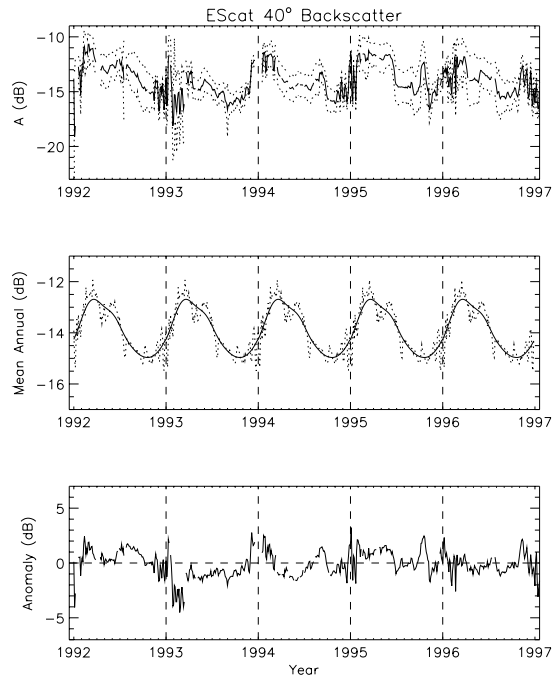


Figure 10. Cumulative surface melt days detected by (a) ERS-2; and (b) NSCAT data during the 1996-97 austral summer season. White areas indicate no melting.

a.



b.

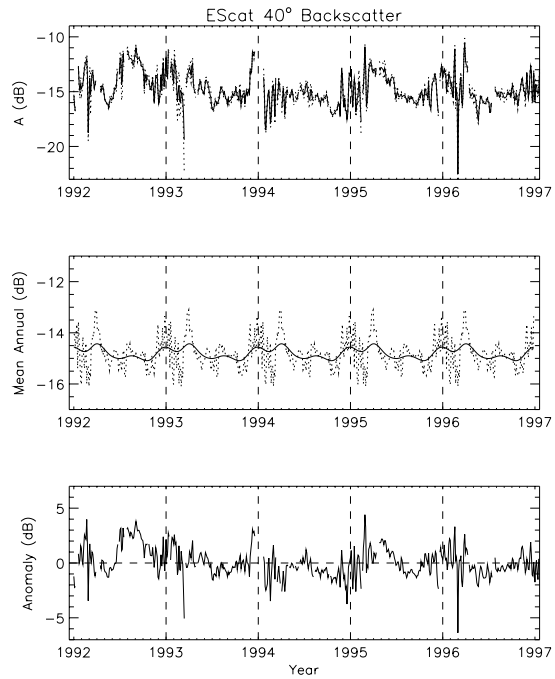


Figure 11. Interannual time series of EScat data from (a) box 9, and (b) box 22. The upper panel in each plot shows the mean A values, with dotted lines indicating a 1σ standard-deviation range. The central panel indicates the mean-annual cycle (dotted) and its six month running mean (solid), and the lowermost panel shows the anomaly cycle resulting from removal of the smoothed mean-annual cycle.

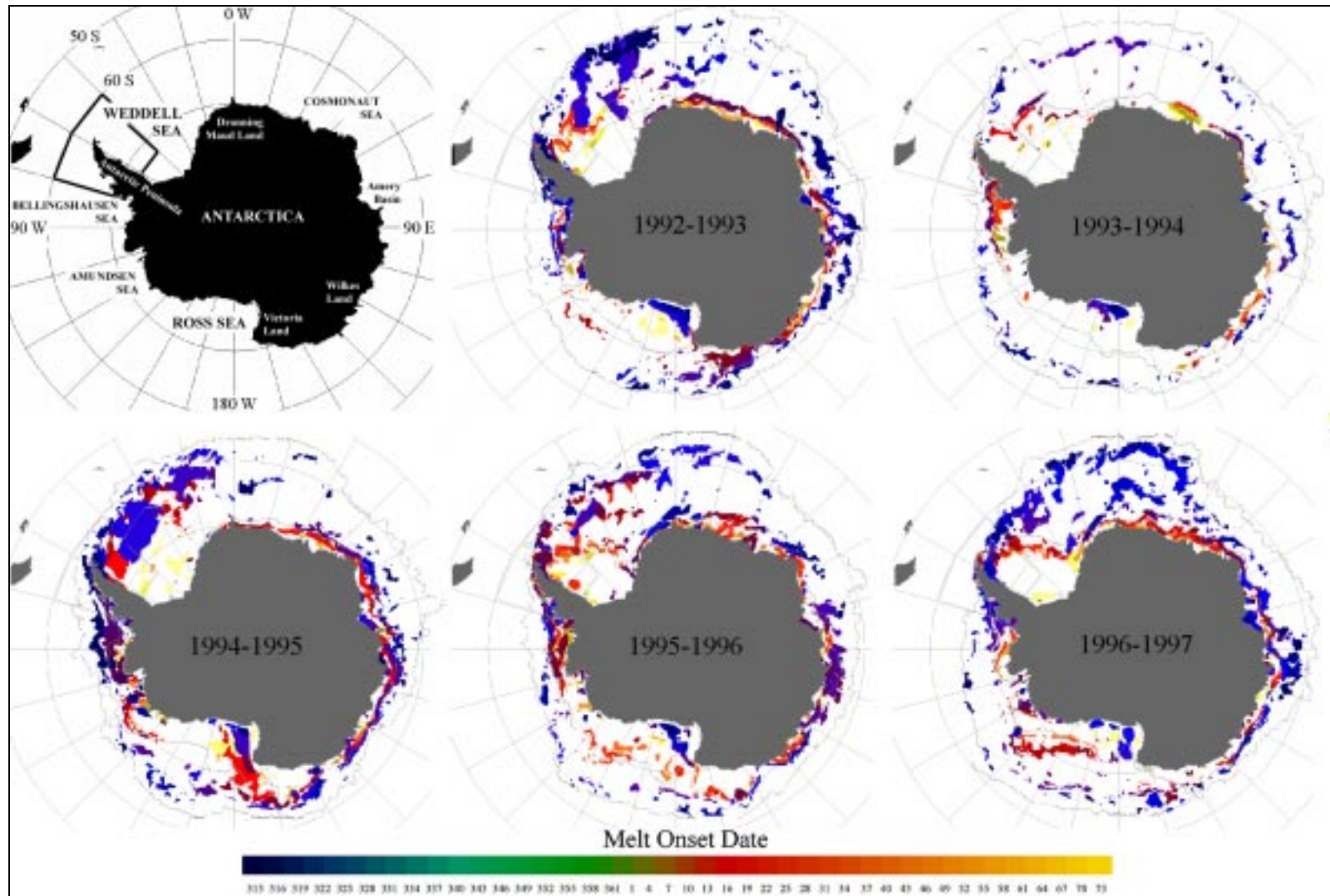


Figure 12. Interannual variability in melt onset for (a) 1992/93, (b) 1993/94, (c) 1994/95, (d) 1995/96, and (e) 1996/97.

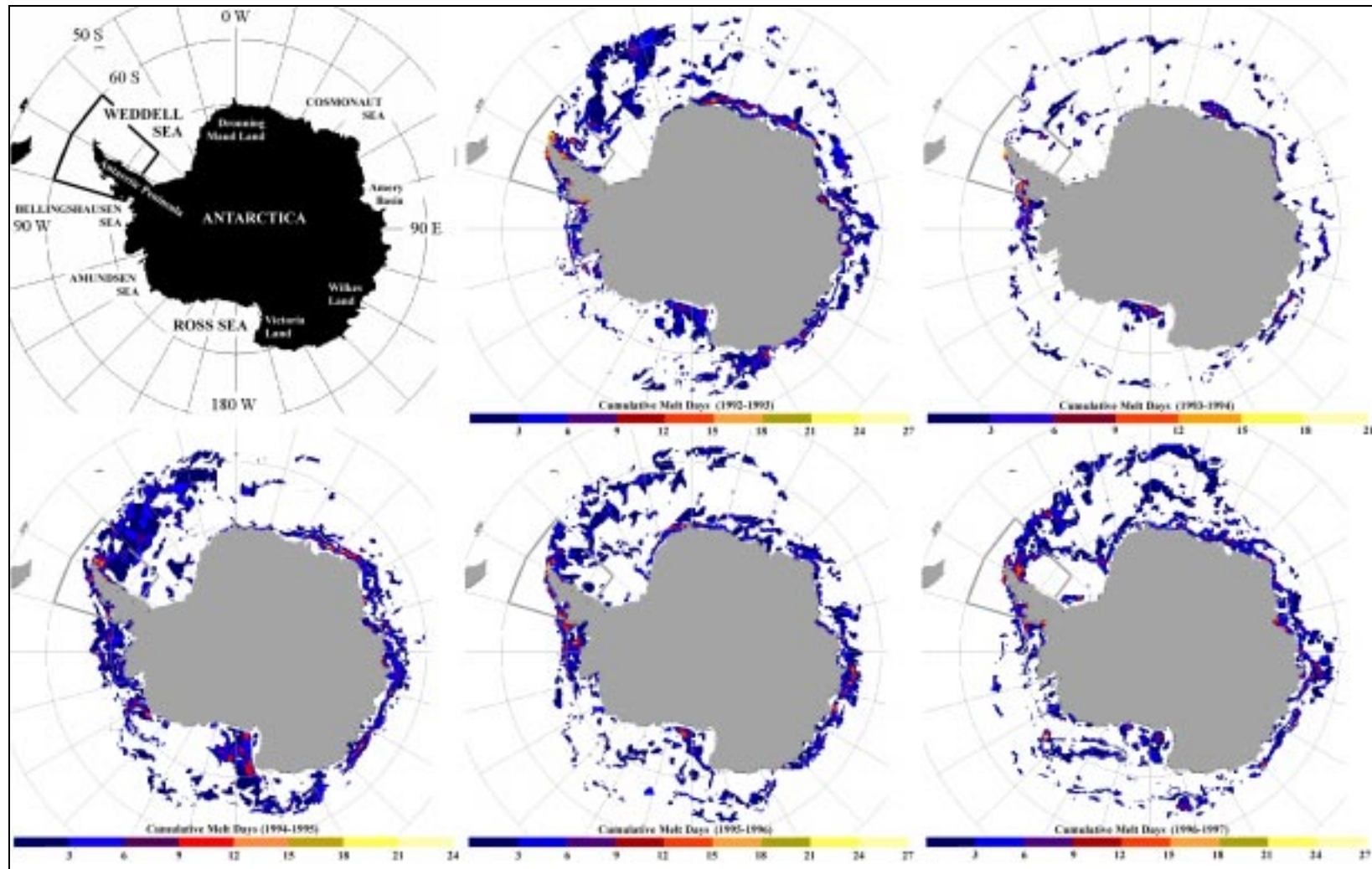


Figure 13. Interannual cumulative melt variability for (a) 1992/93, (b) 1993/94, (c) 1994/95, (d) 1995/96, and (e) 1996/97.